INTERNATIONAL JOURNAL FOR NUMERICAL METHODS IN ENGINEERING
Int. J. Numer. Meth. Engng 2014; **100**:504–533
Published online 29 August 2014 in Wiley Online Library (wileyonlinelibrary.com). DOI: 10.1002/nme.4756

Virtual topography: A fictitious domain approach for analyzing free-surface irregularities in large-scale earthquake ground motion simulation

Doriam Restrepo[1,2,*,†] and Jacobo Bielak[1]

[1]*Department of Civil and Environmental Engineering, Carnegie Mellon University Pittsburgh, Pennsylvania, 15213-3890, USA*
[2]*Now at Departamento de Ingeniería Civil, Universidad EAFIT, Carrera 49 N 7 Sur-50, Medellín, Colombia*

SUMMARY

This paper presents a numerical scheme based on a fictitious domain framework for the numerical modeling of earthquake-induced ground motion in the presence of realistic surface topography of the Earth's crust. We show that by adopting a non-conforming octree-based meshing approach associated with a virtual representation of the surficial irregularity, we can obtain accurate representations of ground motion. From the computational point of view, our methodology proves to be also efficient, and more importantly, it allows us to preserve the salient features of multi-resolution cubic-shaped finite elements for wave propagation applications. We implemented the non-conforming meshing scheme for the treatment of realistic topographies into Hercules, the octree-based finite-element earthquake simulator developed by the Quake Group at Carnegie Mellon University. We tested the benefits of the strategy by benchmarking its results against reference examples, and by means of numerical error estimate analyses. Our qualitative and quantitative comparisons showed a close agreement between our numerical results and the reference results, and also, that the order of convergence of the displacement field is preserved in the presence of surface topography. Moreover, this performance was obtained by using the same mesh refinement techniques with cubic elements as in traditional flat free-surface simulations. Copyright © 2014 John Wiley & Sons, Ltd.

Received 24 February 2014; Revised 19 June 2014; Accepted 6 July 2014

KEY WORDS: fictitious domains; topography; earthquake modeling; octree-based meshes

1. INTRODUCTION

Traditional domain discretization modeling is based upon the premise of a one-to-one correspondence between the body's physical boundaries and its computational representation. With the constantly growing computer capabilities and the highly advanced meshing solvers available, boundary-fitted meshes have been developed for practically every engineering application. By exactly prescribing the solid boundaries, one can readily specify boundary conditions. This is perhaps the most salient feature of boundary-fitted schemes. There are, however, a number of applications where traditional meshing strategies are not the most practical. In fracture mechanics, for instance, meshing imposes a significant computational burden because the mesh must conform to first and second order discontinuities. Moreover, remeshing is often required to track geometric and topological changes as the cracks evolve. This constraint becomes even more demanding if moving discontinuities are present such as in dynamic crack growth simulations. Multiphase materials are also examples where difficulties arise. From reinforced concrete to textiles with complicated patterns, challenges emerge under traditional solid discretization because of the large number of

*Correspondence to: Doriam Restrepo, Departamento de Ingeniería Civil. Universidad EAFIT. Carrera 49 N 7 Sur-50, Medellín, Colombia.
†E-mail: drestre6@eafit.edu.co

inclusions and their highly heterogeneous shapes. Similarly, meshes of realistic geologic settings that exhibit complex topographic features are prone to depend upon tests on Jacobian determinants to ensure positive definiteness before an acceptable mesh is obtained. Because in many applications almost 80% of the overall analysis time is devoted to mesh generation and geometrical analysis [1], the development of quality meshes of complex problems, where computational efficiency is a priority, is still not an easy undertaking.

Strategies to uncouple complex solid boundaries from the domain representation have been proposed since early numerical modeling in the form of non-boundary-fitted meshes. *Meshless* methods, for instance, approximate the solution based on a cluster of scattered nodes throughout the domain. Each node accounts for an influence domain rather than by elements; thus, nodes can be added/removed freely as no connectivity concept is involved (e.g., [2]). Essential boundary conditions are however particularly difficult to handle. Because shape functions do not satisfy the zero-one property, imposing Dirichlet boundary conditions is not as straightforward as in traditional finite elements [3]. Moreover, the method heavily depends upon an optimal location of points near complex geometries, which renders the method computationally burdensome [4, 5]. The generalized finite element modeling (GFEM) [6, 7] and the extended finite element method (XFEM) [8, 9] circumvent inaccuracies of nonconforming meshes by adding a priori information of the

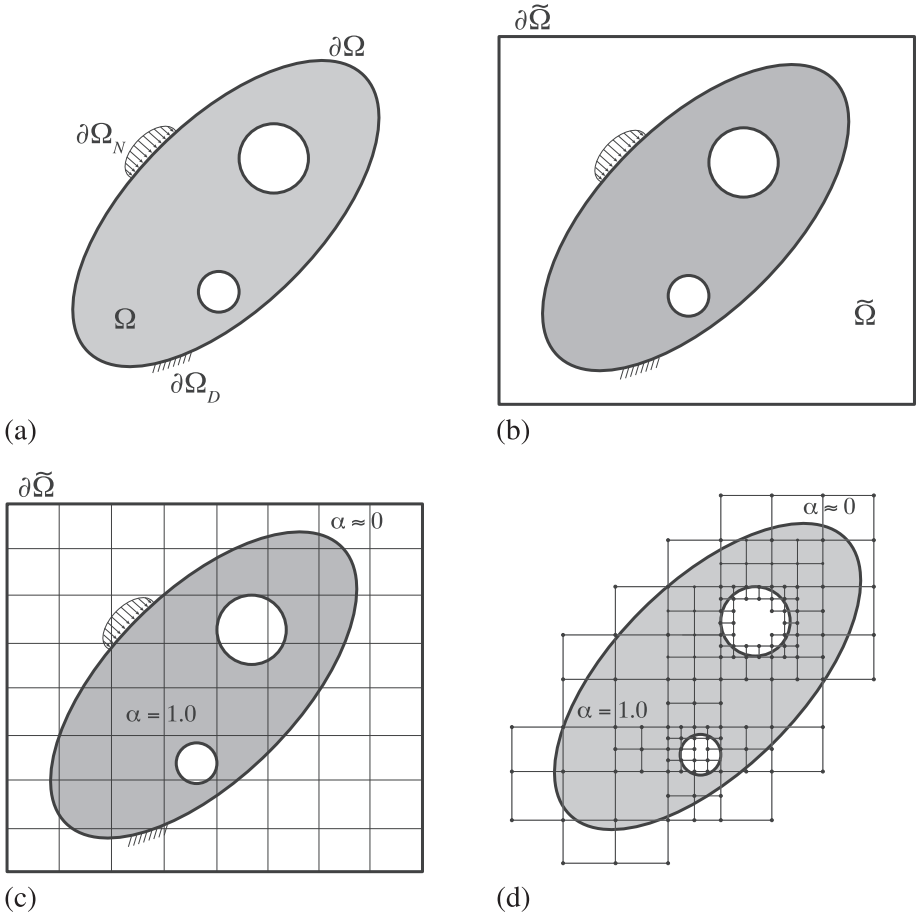

Figure 1. Fictitious domain representation. (a) Targeted domain Ω with external boundary $\partial\Omega = \partial\Omega_N \cup \partial\tilde{\Omega}_D$; $\partial\Omega_N \cap \partial\Omega_D = \emptyset$, where $\partial\Omega_N$ and $\partial\Omega_D$ denote disjoint Neumann and Dirichlet boundaries, respectively. (b) Domain Ω immersed into an augmented body $\tilde{\Omega}$ of regular boundary $\partial\tilde{\Omega}$. (c) Fictitious domain $\tilde{\Omega}$ discretized by a Cartesian mesh of uniform elements. (d) Octree-based finite element mesh discretization scheme for the fictitious domain $\tilde{\Omega}$. Hanging nodes connecting meshes with different levels of refinement are constrained by averaging the displacement field from their anchored nodes as in [15]. Elements completely outside Ω are removed from the mesh.

DOI: 10.1002/nme

functional behavior of the solution to the trial function space by means of partition of unity concepts [10]. The GFEM enriches the approximated global solution with the so-called handbook functions. These special functions are derived from analytical or highly accurate numerical solutions of simplified boundary-value problems that account for the localized features of the actual problem, for example, cracks, material discontinuities, voids (e.g., [11]). On the other hand, the XFEM employs the partition of unity only locally through special functions of a simpler nature added only to the degrees of freedom near the discontinuity. As a result, this gives the XFEM a broader use. GFEM/XFEM ideas are, however, not the most suitable when mesh approximations only emerge because of misalignment with the domain's boundaries because no field enrichment is required in such scenarios.

On the other hand, *fictitious domain* (FD) ideas [12] essentially preserve the same concepts as in traditional finite element modeling (FEM) but dramatically reduce any mesh related geometrical constraints. The basic idea is to embed an intricate body Ω into a simpler shaped one $\tilde{\Omega}$, namely $\Omega \subset \tilde{\Omega}$ (Figure 1(a) and (b)). The augmented body is usually chosen, in 2D, as a rectangle of zero traction on $\partial\tilde{\Omega}$, which is further discretized via voxel-like meshes. The artificial material in the augmented region $\tilde{\Omega} \setminus \Omega$ is penalized by a small α factor, seeking to reduce its contribution to the overall solution and to ensure zero traction condition throughout $\partial\tilde{\Omega}$. Boundary conditions within exterior elements intersecting $\partial\Omega$ are mostly implemented via Lagrange multipliers, although both homogeneous Dirichlet or Neumann boundary conditions throughout $\partial\Omega$ are readily considered through local variations of α, that is, $\alpha = \infty$ and $\alpha = 0$, respectively. To avoid numerical artifacts, some authors have proposed using an artificial material one order of magnitude stiffer than the original material $\alpha = \mathcal{O}(10)$ to approximate homogeneous Dirichlet boundary conditions, while $\alpha = 10^{-10}$ has proven accurate to represent homogeneous Neumann boundary conditions (e.g., [13, 14]). The main feature of the method is that efficient mesh solvers are readily implemented, thus eliminating badly distorted elements and error-prone meshes. Although uniform grids are traditionally employed when finite difference solvers are used (Figure 1(c)), *octree*-finite element approaches are common when one implements finite elements. Thus, the method naturally inherits the main characteristics of multi-resolution finite elements (Figure 1(d)).

In the FD framework then, the approximation of making the solid boundaries non-conforming is shifted to the integration of the weak form of the elements intersecting $\partial\Omega$. Elements completely outside $\partial\Omega$ are simply not considered in any further calculation, while those completely inside are handled conventionally. Available strategies to manage discontinuous integrands range from (1) numerical homogenization techniques (e.g., [16, 17]), (2) decomposition of elements into integration sub-cells (e.g., [7, 18, 19]), (3) quadrature rules at the integration point level (e.g., [20, 21]), or (4) modest low-order trapezoidal integration based on fine grids within each exterior element. These strategies have been widely implemented in 2D stationary problems. 3D simulations, on the other hand, remain challenging. Homogenization techniques generate very fine meshes to capture local variations near material interfaces [22]. Because quadrature rules assume smooth integrands, these demand a large number of Gauss points before an acceptable accuracy is achieved [23]. Octree-adaptive integration schemes are perhaps the most suitable strategies for obtaining accurate formulations. However, these approaches also entail a significant computational effort because quadrature rules need to be employed at each recursive subdivision. In addition, meshes associated with large-scale 3D modeling significantly increase the overall memory demands, as each elemental matrix must be computed and stored independently during the entire simulation. Consequently, deciding on the trade-off between constructing an adequate conforming mesh and performing accurate numerical integrals, as is required in 3D FD modeling, remains challenging.

This paper focuses on providing an alternative solution in a FD framework toward ameliorating the foregoing drawbacks of 3D modeling. Our approach efficiently reduces the computational burden associated with computing discontinuous integrands; it also reduces memory requirements because explicit computation of elemental matrices is avoided. Instead, elemental matrices are computed after scaling template matrices computed at the beginning of the simulation. Although the proposed approach can be applied to a large variety of problems, our main interest is to perform 3D earthquake ground motion simulations including surficial topography. Even while topographic

DOI: 10.1002/nme

site effects have been widely studied through 2D simulations of highly idealized profiles, early numerical research promptly exposed the weaknesses of those oversimplified models, and their inability to draw quantitative conclusions for realistic 3D mountainous regions (e.g., [24–27]). By following a non-conforming meshing scheme for the numerical representation of realistic surficial irregularities, one obviates the treatment of strong localized geometrical variations likely to occur in realistic topographic settings. As a result, peaks, troughs, and re-entrant corners of the targeted relief can be handled readily. Two strategies for generating the finite elements in the neighborhood of the targeted topography are presented. The first strategy is based on a treatment at the integration point level, while the second one can be categorized as a semi-decomposition technique. Theoretically, both strategies are general and can be used in 2D or 3D. Here, we have found that the first strategy works well for 2D problems, but the second one is more suitable in 3D. We implement the 3D strategy using octree-based meshes in Hercules [15], the octree-based finite element parallel software developed by the Quake group at Carnegie Mellon University. This allowed us to use the attractive features of the multi-resolution cubic finite elements. Hercules was originally intended to handle flat free surfaces, using a trilinear finite element spatial discretization, and an explicit central difference scheme in time. This renders a quadratic convergence rate for displacements in both space and time. Numerical experiments considering surficial topography show that quadratic convergence is almost preserved, which brings accuracy and reliability to the method. Moreover, accuracy is attained with the same mesh resolution as in flat-free simulations.

2. CONCEPTUAL FRAMEWORK AND STRATEGY

Consider a homogeneous body Ω bounded by Γ. The boundary Γ is partitioned into two disjoint boundaries such that $\Gamma = \Gamma_N \cup \Gamma_D$; $\Gamma_N \cap \Gamma_D = \emptyset$. We consider homogeneous Dirichlet conditions $\bar{\mathbf{u}}$ on Γ_D, and vanishing tractions along Γ_N. Following FD ideas [12], Ω is immersed into a domain $\tilde{\Omega}$ of regular boundary $\tilde{\Gamma}$ with imposed homogeneous conditions along the Dirichlet $\tilde{\Gamma}_D$ and Neumann $\tilde{\Gamma}_N$ boundaries (Figure 2.)

Suppose that $\tilde{\Omega}$ is filled with a heterogeneous, isotropic, elastic material with variable Lamé properties λ, and μ, while $\tilde{\rho}$ is the mass density of the extended domain. As in standard FEM, the weak form of the elastodynamic equation for the domain $\tilde{\Omega}$ is written as follows:

$$\int_{\tilde{\Omega}} \tilde{\rho}\mathbf{v}\cdot\ddot{\mathbf{u}}\mathrm{d}\tilde{\Omega} + \int_{\tilde{\Omega}} \boldsymbol{\varepsilon}(\mathbf{v}) : \boldsymbol{\sigma}(\mathbf{u})\mathrm{d}\tilde{\Omega} = \int_{\tilde{\Omega}} \mathbf{v}\cdot\mathbf{f}\mathrm{d}\tilde{\Omega}, \tag{1}$$

in which $\mathbf{v}$ and $\mathbf{u}$ denote the test and trial functions, and $\mathbf{f}$ represents the body forces that are restricted to lie within Ω. $\boldsymbol{\sigma}$ and $\boldsymbol{\varepsilon}$ are the second order stress and strain tensors, respectively. Under the assumption of small strains, the kinematic equation is given by

$$\boldsymbol{\varepsilon}(\mathbf{u}) = \nabla_s \mathbf{u}, \tag{2}$$

where ∇_s is the symmetric part of the gradient operator. We model the material in $\tilde{\Omega}$ as an isotropic, heterogeneous, elastic solid. The stress and strain vector fields are then related through the elastic

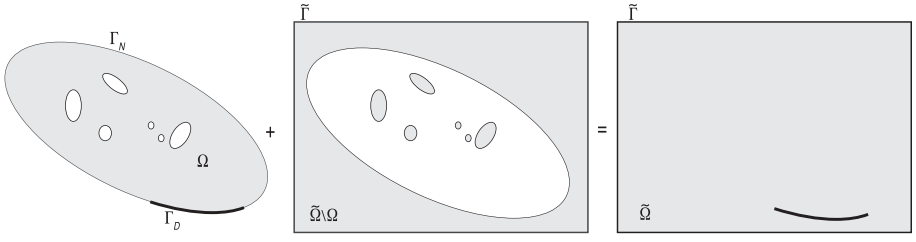

Figure 2. Domain Ω with external boundary $\Gamma = \Gamma_N \cup \Gamma_D$ immersed into a domain $\tilde{\Omega}$ of regular boundary $\tilde{\Gamma}$ partitioned into two disjoint boundaries such that $\tilde{\Gamma} = \tilde{\Gamma}_N \cup \tilde{\Gamma}_D$; $\tilde{\Gamma}_N \cap \tilde{\Gamma}_D = \emptyset$.

DOI: 10.1002/nme

material tensor $\mathbf{C}$ and the penalty factor α as

$$\begin{aligned}\boldsymbol{\sigma}(\mathbf{u}) &= \alpha(\mathbf{x})\mathbf{C}\colon\boldsymbol{\varepsilon}(\mathbf{u})\\ \alpha &= \begin{cases} 1 & \forall\ \mathbf{x}\in\Omega \\ 10^{-p} & \forall\ \mathbf{x}\in\tilde{\Omega}\setminus\Omega. \end{cases}\end{aligned} \tag{3}$$

The exponent p is chosen small enough to mimic internal voids and holes but sufficiently large to ensure numerical stability. Values of p ranging between 3 and 14 have been used successfully (e.g., [13, 14, 28]). In this paper, we use only limiting values 0 and 1 for α. $\mathbf{C}$ is the fourth order tensor of elastic constants, which for an isotropic elastic material can be expressed in Cartesian coordinates as

$$C_{ijkl} = \lambda\delta_{ij}\delta_{kl} + \mu\left(\delta_{ik}\delta_{jl} + \delta_{il}\delta_{jk}\right). \tag{4}$$

In addition, we extend the penalty factor concept to redefine the material density of $\tilde{\Omega}$ in terms of the density ρ of the original domain Ω

$$\tilde{\rho} = \alpha\rho. \tag{5}$$

Thus, the penalty factor α modulates both stiffness and inertia throughout the system. It is readily seen that by writing down the variational problem in (1) as contributions from Ω and $\Omega\setminus\tilde{\Omega}$, and adopting the limiting value of $\alpha = 0$, as well as the traction-free condition throughout $\tilde{\Gamma}_N$, one retrieves the weak form of the targeted domain Ω. That is for $\alpha \neq 0$:

$$\begin{aligned}&\int_\Omega \rho\mathbf{v}\cdot\ddot{\mathbf{u}}\mathrm{d}\Omega + \alpha\int_{\tilde{\Omega}\setminus\Omega}\rho\mathbf{v}\cdot\ddot{\mathbf{u}}\mathrm{d}\Omega + \int_\Omega \boldsymbol{\varepsilon}(\mathbf{v}):\boldsymbol{\sigma}(\mathbf{u})\mathrm{d}\Omega + \alpha\int_{\tilde{\Omega}\setminus\Omega}\boldsymbol{\varepsilon}(\mathbf{v}):\boldsymbol{\sigma}(\mathbf{u})\mathrm{d}\Omega\\ &= \int_\Omega \mathbf{v}\cdot\mathbf{f}\mathrm{d}\Omega + \alpha\int_{\tilde{\Omega}\setminus\Omega}\mathbf{v}\cdot\mathbf{f}\mathrm{d}\tilde{\Omega},\end{aligned}$$

and for $\alpha = 0$:

$$\int_\Omega \rho\mathbf{v}\cdot\ddot{\mathbf{u}}\mathrm{d}\Omega + \int_\Omega \boldsymbol{\varepsilon}(\mathbf{v}):\boldsymbol{\sigma}(\mathbf{u})\mathrm{d}\Omega = \int_\Omega \mathbf{v}\cdot\mathbf{f}\mathrm{d}\Omega. \tag{6}$$

To obtain a discrete representation of (1), it is assumed that $\tilde{\Omega}$ can be represented in terms of a set of non-overlapping cubic elements $\tilde{\Omega}_e$ of the type shown in Figure 1(d), such that

$$\sum_e\left(\int_{\tilde{\Omega}_e}\tilde{\rho}\mathbf{v}\cdot\ddot{\mathbf{u}}\mathrm{d}\tilde{\Omega}_e + \int_{\tilde{\Omega}_e}\boldsymbol{\varepsilon}(\mathbf{v}):\boldsymbol{\sigma}(\mathbf{u})\mathrm{d}\tilde{\Omega}_e - \int_{\tilde{\Omega}_e}\mathbf{v}\cdot\mathbf{f}\mathrm{d}\tilde{\Omega}_e\right) = 0. \tag{7}$$

Adopting standard finite element ideas, the trial function is defined as follows:

$$\mathbf{u}(\mathbf{x},t) = \sum_{n\in N}\phi_n(\mathbf{x})\mathbf{u}_n(t), \tag{8}$$

in which N is the set of all the nodes in the mesh, $\phi_n(\mathbf{x})$ is the standard finite element global basis function associated with the n-th node, and $\mathbf{u}_n$ are vectorial time-dependent degrees of freedom at node n. Notice that the penalized material assumption (3) is numerically equivalent to considering a discontinuous displacement field $\mathbf{u}(\mathbf{x},t)$ of the form

$$\mathbf{u}(\mathbf{x},t) = \sum_{n\in N}\sqrt{\alpha(\mathbf{x})}\phi_n(\mathbf{x})\mathbf{u}_n(t)\ , \tag{9}$$

DOI: 10.1002/nme

which allows one to redefine the global shape and trial functions as

$$\psi_n(\mathbf{x}) = \sqrt{\alpha(\mathbf{x})}\phi_n(\mathbf{x}), \tag{10}$$

$$\mathbf{u}(\mathbf{x}, t) = \sum_{n \in N} \psi_n(\mathbf{x})\mathbf{u}_n(t). \tag{11}$$

Using (11) as the trial function in a spatial Galerkin semi-discretization by finite elements of (1), one obtains a system of ordinary differential equations of the form

$$\mathbf{M}\ddot{\mathbf{U}} + \mathbf{K}\mathbf{U} = \mathbf{P}, \tag{12}$$

in which $\mathbf{M}$ and $\mathbf{K}$ are the sparse mass and stiffness matrices, $\mathbf{P}$ is the global nodal vector of effective forces, and $\mathbf{U}$ is the global vector of nodal displacements. The elements of the matrices $\mathbf{M}$ and $\mathbf{K}$ are as follows:

$$\mathbf{M}_{ij} = \int_{\tilde{\Omega}} \tilde{\rho}\psi_i \psi_j \mathbf{I} \mathrm{d}\tilde{\Omega}, \tag{13}$$

$$\mathbf{K}_{ij} = \int_{\tilde{\Omega}} (\mu + \lambda)\nabla\psi_i \nabla\psi_j^{\mathsf{T}} \mathrm{d}\tilde{\Omega} + \int_{\tilde{\Omega}} \mu \nabla\psi_i^{\mathsf{T}} \nabla\psi_j \mathbf{I} \mathrm{d}\tilde{\Omega}. \tag{14}$$

Equations (13) and (14) preserve the conventional form encountered in a standard linear elastodynamics FEM framework (e.g., 29). More important, because of the use of the material function $\alpha(\mathbf{x})$, Equations (13) and (14) properly handle the actual boundary of the domain and the traction-free condition in Γ. For elements with nodes within Ω, both expressions reduce to those from the classical finite element scheme because $\alpha(\mathbf{x}) = 1$. For elements with external nodes, Equations (13) and (14) are still valid as long as the integrals are evaluated over the actual portions of Ω enclosed by the cube-shaped finite element. As is readily seen, the treatment of voids, holes, and traction-free surfaces by FD ideas renders the same result as in the classical finite element framework as long as the zones of empty material in the element are excluded from the integral of the weak form. However, because the displacement field is expressed in terms of physical and non-physical nodes, the numerical scheme cannot strictly be denoted as an ordinary finite element analysis.

2.1. Numerical integration: quadrature rule approach

Inherent to non-conforming meshing schemes is the evaluation of discontinuous integrands. The evaluation of (13) and (14) has traditionally been computed numerically using standard quadrature rules. For interior elements, the numerical integration is straightforward. Moreover, because internal elements are cubes (squares in 2D), the stiffness and mass matrices need to be computed for a single element and scaled according to the size and material properties of the individual elements. For external elements, on the other hand, the mass and stiffness matrices must be computed separately for each element due to variations of $\alpha(\mathbf{x})$ in elements that intersect Γ. The main idea is then to use a sufficient number of Gauss points to achieve proper accuracy.

Reference [20, 21] provided insight regarding the accuracy of quadrature rules when dealing with discontinuous functions. They expressed the error bound in the integration of a discontinuous function by the largest quadrature weight w_i and the maximum distance $\zeta_i - \zeta_{i+1}$ between two neighboring Gauss points. For the 1D case, using a least-square fit, they reported an error bound of the form

$$\text{error bound} \approx 5.07G^{-1.82}, \tag{15}$$

where G is the number of quadrature points. The extension to the 3D case is straightforward. The corresponding errors are shown in Table I.

By using an adequate number of Gauss points, integrals such as those in (13) and (14) can be computed accurately. Other authors have also used uniform quadrature schemes of high

DOI: 10.1002/nme

Table I. Integration error bound behavior for a 3D step function discontinuity. After [20].

Gauss rule	Error bound(%) = $\frac{(5.07G^{-1.82})^3}{8} \times 100\%$
$2 \times 2 \times 2$	37
$3 \times 3 \times 3$	4
$4 \times 4 \times 4$	0.8
$5 \times 5 \times 5$	0.2
$10 \times 10 \times 10$	0.006

degree to compute discontinuous integrands at the expense of lowering the convergence rate (e.g., [13, 30, 31]). For 2D modeling, this approach is still attractive, especially with the current computational capabilities. This is particularly true for 2D earthquake modeling, including surficial topography, where the number of topography intersected elements is small compared with that of the interior ones; thus, one can afford the computational cost of computing and storing on the fly the stiffness and mass matrices of the topographic elements. Evidence of the applicability and the reliability of the proposed numerical scheme was presented also in the framework of 3D soil-structure numerical modeling by [32], although under flat-free conditions. These authors concluded that finite elements with material discontinuities treated at the point integration level accurately represent the characteristics of the soil profile and can be used to predict the dynamic response of building structures when subjected to earthquake ground excitation in soft soils.

2.2. *Numerical integration: virtual topography scheme*

The error bounds cited in the previous section provide a convenient way to deal with integrals that involve discontinuous functions. This approach, however, has two drawbacks when used at the free surface of 3D large-scale realistic situations. First, because each exterior finite element encloses a different portion of the topography within, each stiffness and mass matrix must be computed and stored independently. This affects the overall computational efficiency and simulation time. Second, in cases where any exterior finite element covers only a small portion of the topography, strong numerical artifacts appear because of the small lumped mass values linked to the element nodes. Therefore, the required time step in the numerical integration scheme is greatly reduced. To avoid this difficulty, this work follows an alternative strategy for 3D problems, which we denote as *virtual topography* (VT). The idea is to further divide each exterior topographic element into tetrahedral elements. Of particular interest due to the similarities in splitting octree-based meshes are the studies of [33] and [34]. The former combine a unit cell homogenization technique together with octree-based meshes in an FEM framework to predict the mechanical behavior of woven composite textiles, while [34] combine an octree-based mesh with separate tetrahedral elements that conform to the free-surfaces and layer interfaces. Our approach, however, is neither intended to generate particular zones of conforming tetrahedra, nor to follow a decomposition scheme where elements are partitioned into sub-domains that align with the domain boundaries in order to carry out the integrals. Our local partition scheme specifically divides a topography intersected cubic element into five, linear, still non-conforming tetrahedra in order to better approximate the geometry and mechanical contribution of the topographic feature (Figure 3).

The proposed partition ensures that no additional nodes are created within each parent cube. Additionally, it is also clear that empty tetrahedra are eliminated from any further consideration; this increases numerical stability. The division at the topographic element level admits writing down the local stiffness matrix of the exterior element $\mathbf{k}_{ij}$ as the contribution from its five tetrahedral elements:

$$\mathbf{k}_{ij} = \sum_{s=1}^{5} \int_{\Omega_s} (\mu + \lambda) \nabla \chi_i \nabla \chi_j^{\mathsf{T}} \mathrm{d}\Omega_s + \int_{\Omega_s} \mu \nabla \chi_i^{\mathsf{T}} \nabla \chi_j \mathbf{I} \mathrm{d}\Omega_s, \tag{16}$$

where χ_i are local trial functions, and it is understood that the summation symbol in (16) stands for the proper assembly of each tetrahedron contribution to the cubic element stiffness.

DOI: 10.1002/nme

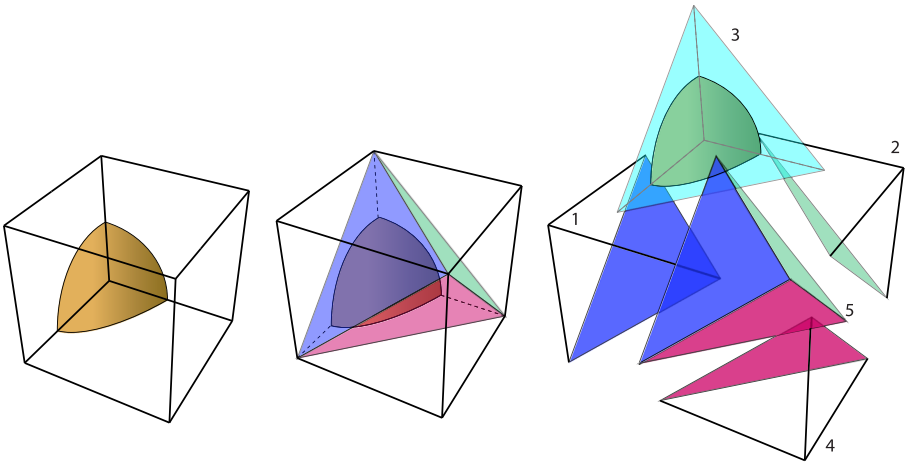

Figure 3. Cubic topographic element partitioned into five non-conforming linear tetrahedral elements.

The most attractive feature of such a partition is related to the calculation of the stiffness matrices in (14). Because each tetrahedron is linear, gradients in (16) are constants. The material properties, on the other hand, could be variable within each parent cubic element. In addition, the tetrahedra could exhibit material discontinuities, that is, interfaces between different homogeneous materials. In 3D earthquake modeling of realistic regions, material parametrization has been traditionally implemented by harmonic and arithmetic averaging of rigidity and density [35, 36]. Here, we adopt an arithmetic averaging of both density and rigidity, which translates into implicitly modeling material discontinuities, and accepting a first order error in the solution. Verification studies have shown, however, that such a simplification is acceptable and only renders minor differences in 3D earthquake modeling (e.g., [37]). Therefore, taking λ and μ as constants within each element, the evaluation of the stiffness integrals reduces merely to computing the volume occupied by each tetrahedron.

$$\mathbf{k}_{ij} = \sum_{s=1}^{5} \Big((\mu + \lambda) \nabla \chi_i \nabla \chi_j^{\mathsf{T}} + \mu \nabla \chi_i^{\mathsf{T}} \nabla \chi_j \mathbf{I} \Big)_s \int_{\Omega_s} \mathrm{d}\Omega_s. \tag{17}$$

Multiplying and dividing (17) by the full volume of each tetrahedron Ω_s gives the following:

$$\mathbf{k}_{ij} = \sum_{s=1}^{5} \left[\Big((\mu + \lambda) \nabla \chi_i \nabla \chi_j^{\mathsf{T}} + \mu \nabla \chi_i^{\mathsf{T}} \nabla \chi_j \mathbf{I} \Big)_s \, \Omega_s \right] \frac{\int_{\Omega_s} \mathrm{d}\Omega_s}{\Omega_s}. \tag{18}$$

The first factor in (18) is the complete stiffness matrix of the tetrahedron s, while the second term represents its void ratio $\varphi_s = \frac{\int_{\Omega_s} \mathrm{d}\Omega_s}{\Omega_s}$.

$$\mathbf{k}_{ij} = \sum_{s=1}^{5} \mathbf{k}_s^{\mathrm{FullTetrh}} \varphi_s. \tag{19}$$

From (19), it is clear that empty tetrahedral elements will be automatically ruled out by φ as is intuitively expected, while the degree of participation of the remaining tetrahedra will be completely controlled by their void ratios. Gauss quadrature rules are then needed only to compute these void ratios. There is still another very important feature of (19). Because the void ratio modulates the contribution of each individual tetrahedron, (19) shows that even for the case of irregular topography, the scalability of the octree-based approach still holds.

2.3. Lumped mass strategy

Explicit step-by-step time integration methods have proven to be a reliable scheme for modeling structures in transient wave propagation. It is also well known that the efficiency of explicit time

DOI: 10.1002/nme

integration schemes such as the central difference method relies upon lumped mass techniques. By lumping the mass, the discrete representation of the balance equation does not involve the solution of any system of equations; thus, the computational cost is greatly reduced. In related numerical strategies such as in the XFEM, the first attempt at lumping the mass matrix was carried out by [38]. By exactly preserving the kinetic energy of the element to rigid body motions, and assuming a lumped mass matrix of constant terms, the lumped mass value of the enriched nodes m_{diag} was expressed as follows:

$$m_{\text{diag}} = \frac{m}{n_{\text{nodes}}} \frac{1}{\tilde{\Omega}_e} \int_{\tilde{\Omega}_e} g^2(\mathbf{x}) \mathrm{d}\tilde{\Omega}_e, \tag{20}$$

where m is the mass of the element, n_{nodes} is the element's number of nodes, $\tilde{\Omega}_e$ represents the volume (in 3D), area (in 2D), or length (in 1D) of the element, and $g(\mathbf{x})$ is the so-called XFEM enrichment function. Because (20) was developed for elements completely filled with matter, it cannot be used for elements intersected by free surfaces without further modification. More recently, [39] revisited (20) for a discontinuous displacement field such as in (11). By adopting the same energy ideas as in [38], they showed that the lumped mass matrix for an exterior element can be readily obtained by multiplying the material fraction of the element by the lumped mass of the same element without discontinuity. Similar ideas were proposed by [40] for lumping the mass matrix of constant strain elements in the presence of voids. Consequently, scalability is also preserved for the mass matrix:

$$\mathbf{m}_{ij} = \sum_{s=1}^{5} \mathbf{m}_s^{\text{FullTetrh}} \varphi_s. \tag{21}$$

In (21), $\mathbf{m}_s^{\text{FullTetrh}}$ represents the lumped mass matrix of the full tetrahedron, which can be computed by the row-sum technique or by the widely used lumping method in which the nodal-mass is obtained by evenly distributing the material mass between the four nodes of the tetrahedron. We adopt this lumping technique in the present work.

2.4. Time step

As stated previously, we use the second-order central difference method to integrate the semi-discretized (12) step-by-step. Because this method is only conditionally stable, one must choose a time step Δt that satisfies the Courant–Friedrichs–Lewy condition. Under the absence of damping, this condition is

$$\Delta t < \Delta t_{crit} = \frac{2}{\omega_{max}}, \tag{22}$$

where ω_{max} is the maximum natural frequency of the system. In practice, ω_{max} is related to the highest eigenvalue of each mesh element taken independently. For conventional octree-based meshes, Δt is often taken as

$$\Delta t = c * \min\left(\frac{\Delta \mathrm{x}}{V_p}\right), \tag{23}$$

where Δx and V_p stand for the element's size and P-wave velocity, respectively. c represents the Courant number, usually between 0.3 and 0.4 [41].

In general, the maximum eigenvalue in the whole mesh controls the time-step. In our non-conforming meshing scheme, this maximum will be usually associated with the tetrahedron with the smallest material volume enclosed. The main concern is that these eigenvalues might be very small because the nodal lumped mass depends on the location of the enclosed volume. A closer look at the eigenvalue problem shows, however, that the fundamental modes ϕ_s and frequencies ω_s of the s tetrahedron are independent of its matter content [40]. Writing down the eigenvalue equation for any given tetrahedron s, one obtains the following:

$$\left(\mathbf{k}_s^{\text{FullTetrh}} \varphi_s - \omega_s^2 \mathbf{m}_s^{\text{FullTetrh}} \varphi_s\right) \phi_s = 0. \tag{24}$$

DOI: 10.1002/nme

From (24), it is readily seen that both stiffness and mass matrices are scaled by φ_s, thus the fundamental frequencies and modal shapes of the partially filled tetrahedron match exactly those of the full tetrahedron

$$\left(\mathbf{k}_s^{\text{FullTetrh}} - \omega_s^2 \mathbf{m}_s^{\text{FullTetrh}}\right) \phi_s = 0. \tag{25}$$

Consequently, in VT, the time step is independent of the material fraction within the domain and is approximated by the traditional value given by (23). This is an important feature of the adopted mass lumping procedure.

3. NUMERICAL EXAMPLES: 2D VERIFICATION

In this section, we illustrate the partial Gauss-integration methodology by two simple numerical experiments with idealized surficial irregularities in a 2D homogeneous half-space. A Rayleigh wave is chosen to represent the incident wavefield because surficial irregularities have a larger effect in the propagation of surface waves than of body waves due to the difference in their travel paths [42]. Additionally, because Rayleigh waves present a more challenging scenario physically and numerically than incident body waves, this offers a more severe test of the performance of the proposed numerical framework.

Classical Lysmer-Kuhlemeyer [43] absorbing boundaries were implemented in all of the boundaries, except on the free surface of the domain; material damping is omitted for simplicity. A mass threshold (MTR) is imposed on the external elements to avoid numerical artifacts. That is, if the mass of the real portion of the domain contained within an external element is smaller than MTR, this element will not be considered as part of the simulation domain. Results from the proposed methodology are compared with those obtained using DAMIAN [44], a general 2D boundary element method (BEM) tool developed by the Applied Mechanics Research Group at the Universidad EAFIT (Medellín, Colombia) for modeling seismic-wave propagation and earthquake ground motion in homogeneous 2D regions.

In both simulations, an incident Rayleigh wave traveling from the left side of the domain as a Ricker wavelet in time with characteristic frequency $f_c = 1$ Hz is considered as the seismic excitation. The incident wavelet is normalized in such a way that its horizontal component coincides with the shape of the Ricker pulse. The FEM and BEM meshes were discretized according to

$$\Delta \mathrm{x} = \frac{V_s}{f_{\max} \mathrm{PPW}}. \tag{26}$$

Equation (26) is expressed in terms of the S-wave velocity, V_s, of the domain, the maximum frequency of the simulation $f_{\max}$, and the number of points per wavelength (PPW). The Courant-Friedrichs-Lewy CFL condition of stability is guaranteed for the FEM simulation by using a time step:

$$\Delta t = \frac{\Delta \mathrm{x}}{3V_p}, \tag{27}$$

where V_p is the P-wave velocity of the domain. This requirement is not needed for the BEM formulation although it was kept for consistency.

3.1. Semi-circular hill over a homogeneous half-space

Figure 4 illustrates a homogeneous semi-circular hill of radius equal to the minimum wavelength $\lambda_{\min} = \lambda = V_s / f_{\max}$ of the incoming wave and the dimensions of the computational domain used for the analysis. Numerical experiments have shown that the dimensions of the truncated domain in Figure 4 reduce the occurrence of spurious reflections from the local Lysmer-Kuhlemeyer absorbing boundaries. Figure 5 shows a detailed view of the FEM mesh of the sub-region of interest corresponding to PPW = 10 (10PPW). The blue solid line represents the target shape of

DOI: 10.1002/nme

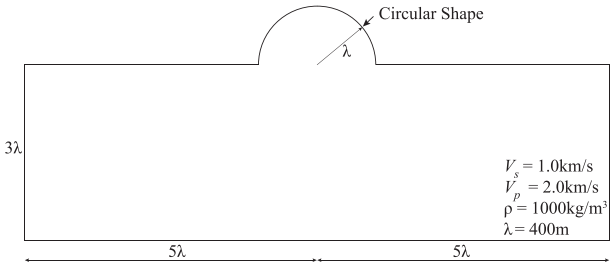

Figure 4. Computational domain of the semi-circular hill over homogeneous half-space.

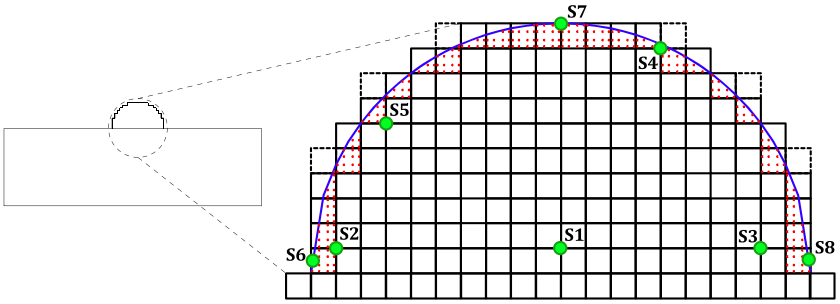

Figure 5. FEM mesh at the region of interest corresponding to the 10PPW–4G–25MTR simulation. Red dots illustrate the quadrature points used for the numerical integration at the external elements. Green dots represent the selected internal receivers. Dotted squares represent the disregarded elements due to MTR $=$ 25%.

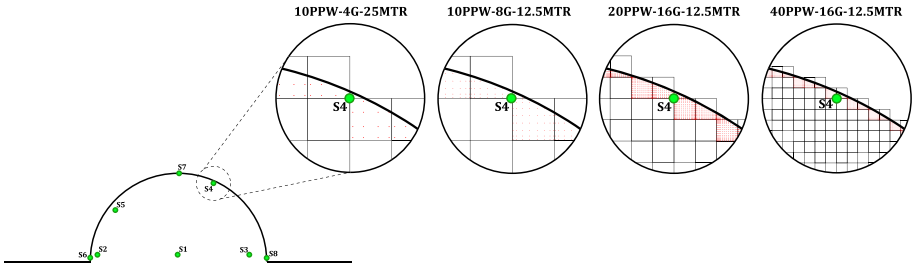

Figure 6. Augmented views of meshes exhibiting different levels of refinement near station S4. The left magnified view depicts a mesh tailor made to accommodate 10 points per wavelength (10PPW) in conjunction with a 4×4 Gauss quadrature rule (4G) and a 25% mass-threshold (25MTR). In the middle-left is the mesh resolution corresponding to 10PPW, 8G, and 12.5MTR. In the middle-right is the mesh resolution for 20PPW, 16G, and 12.5MTR. The right view depicts a segment of the 40PPW, 16G, 12.5MTR mesh in the neighborhood of station S4.

the semi-circular hill. The small red dots illustrate the 4×4 Gauss quadrature rule (4G), implemented for the numerical integration of Equations (13) and (14) at the external elements. The error bound associated with the numerical integration scheme is $\approx$ 4% according to the 2D version of (15). This error can be easily reduced just by increasing the number of Gauss points. We assumed MTR $=$ 25% (25 MTR). Although this constraint might seem severe, only four elements are eliminated because of such a restriction (see dotted squares in Figure 5). Furthermore, aiming at providing evidence of the impact of the mesh variables in the overall response of the domain, we simulated the domain under three additional combinations of MTR, G, and PPW, namely 10PPW–8G–12.5MTR; 20PPW–16G–12.5MTR; and 40PPW–16G–12.5MTR. Figure 6 illustrates augmented views near station S4 for the whole set of simulations. Receivers are denoted by the large green dots S1, S2, . . . , S8.

DOI: 10.1002/nme

Results for the horizontal U_x and vertical U_z components of ground displacement at the selected stations are shown in Figure 7. Blue lines illustrate the results from the 10PPW–4G–25MTR simulation, green lines from the 10PPW–8G–12.5MTR results, while cyan and yellow lines depict results from the 20PPW–16G–12.5MTR, and the 40PPW–16G–12.5MTR mesh conditions. Dotted red lines show the results from the BEM numerical scheme. Good agreement in the results can be observed for most of the stations. The proposed strategy, for instance, reproduces almost wiggle-by-wiggle the response from the BEM formulation during the strong phase of the synthetics at all the stations near the base. Notice that the FEM time histories exhibit an almost exact overlap regardless of the mesh resolution parameters employed. In particular, there is no significant difference between using MTR = 25% or 12.5% for this example. This agreement is achieved even at the free surface stations, that is, S6, S7, and S8. Thus, our simulations show that for these particular receivers, convergence is achieved at a very low cost. This might be correlated with the intrinsic smoothness of the hill, thus the tendency to lowering diffraction effects. For station S4, a wiggle-by-wiggle agreement with BEM results is still visible for the horizontal component of displacement. For the vertical component, good qualitative agreement is achieved, although the proposed strategy slightly overpredicts the maximum response at the specified location. However, the comparison between results from increasingly refined meshes allows us to conclude that the FEM results correspond to the correct solution, and that the BEM solution slightly under predicts the response at station S4, possibly because the BEM solution is taken to be piecewise constant within each element.

Figure 8 presents the peak ground displacement (PGD) for the two components along the free surface, and normalized with respect to the corresponding component of the incident wave. The circular hill divides naturally the free surface into three regions. Results on the left side ($x/\lambda \leqslant -1$) show variations only within one wavelength from the left foothill. In this zone, a mild amplification in both components is present at $x/\lambda \approx -1.5$. The largest effects occur at the left foot with an almost constant reduction of 0.7 for both components. On the hill ($-1 \leqslant x/\lambda \leqslant 1$), large reductions/amplifications and strong spatial variability are observed. At the top the vertical PGD is strongly reduced to 30% of the vertical component of the incident field, while the horizontal PGD only experiences a modest amplification of 16% with respect to the incident component. The largest amplification of the horizontal component (1.5) occurs at about $x/\lambda \approx 1.5$ to the right of the hilltop. This shifting of the PGD from the hilltop is in agreement with results from previous studies (e.g., [45]). Finally, on the right hand side of the foothill ($x/\lambda \geqslant 1$), a noticeable shielding effect is observed, such as that reported by [42]. Here, both PGD values are reduced, with larger changes once again close to the foot of the mountain and more evident for the horizontal component.

Further insight into the effect of the topographic system on the response can be gained by filtering-out the effects of the excitation using results in the frequency domain. Figure 9 presents plots of frequency response as transfer functions (TF) relative to the amplitude of the incoming wave for the two displacement components. These TF are presented as 2D contours of amplitude in terms of both frequency and location throughout the free surface. The 2D representations clearly depict spatial patterns of amplification. Such amplification greatly depends upon the position of the receiver. Over the reflected region ($x/\lambda \leqslant -1$) both components of displacement exhibit a stripe-like spatial pattern. For each frequency, the TFs exhibit several peaks and troughs. Some of the peaks in the vertical component are clearly associated with resonance frequencies. The spatial variation appears also to be more complex for the vertical component, although with smaller amplification than for the horizontal results. Within the interior region $-1 \leqslant x/\lambda \leqslant 1$, two resonance frequencies are clearly distinguishable in the horizontal component contour, $f \approx 0.35$ Hz, and $f \approx 1.5$ Hz. Notice that $f \approx 1.5$ Hz is the frequency associated with the amplification of the horizontal component at ($x/\lambda \approx 0.5$). In the transmitted region ($x/\lambda \geqslant 1$), some moderate diagonal stripes are present. The low and almost constant amplitude is evidence of (1) the shield effect of the hill and (2) a Rayleigh-like transmitted phase. In either case, the transmitted phases are substantially reduced by the topography, even at the receivers located near the foothill.

DOI: 10.1002/nme

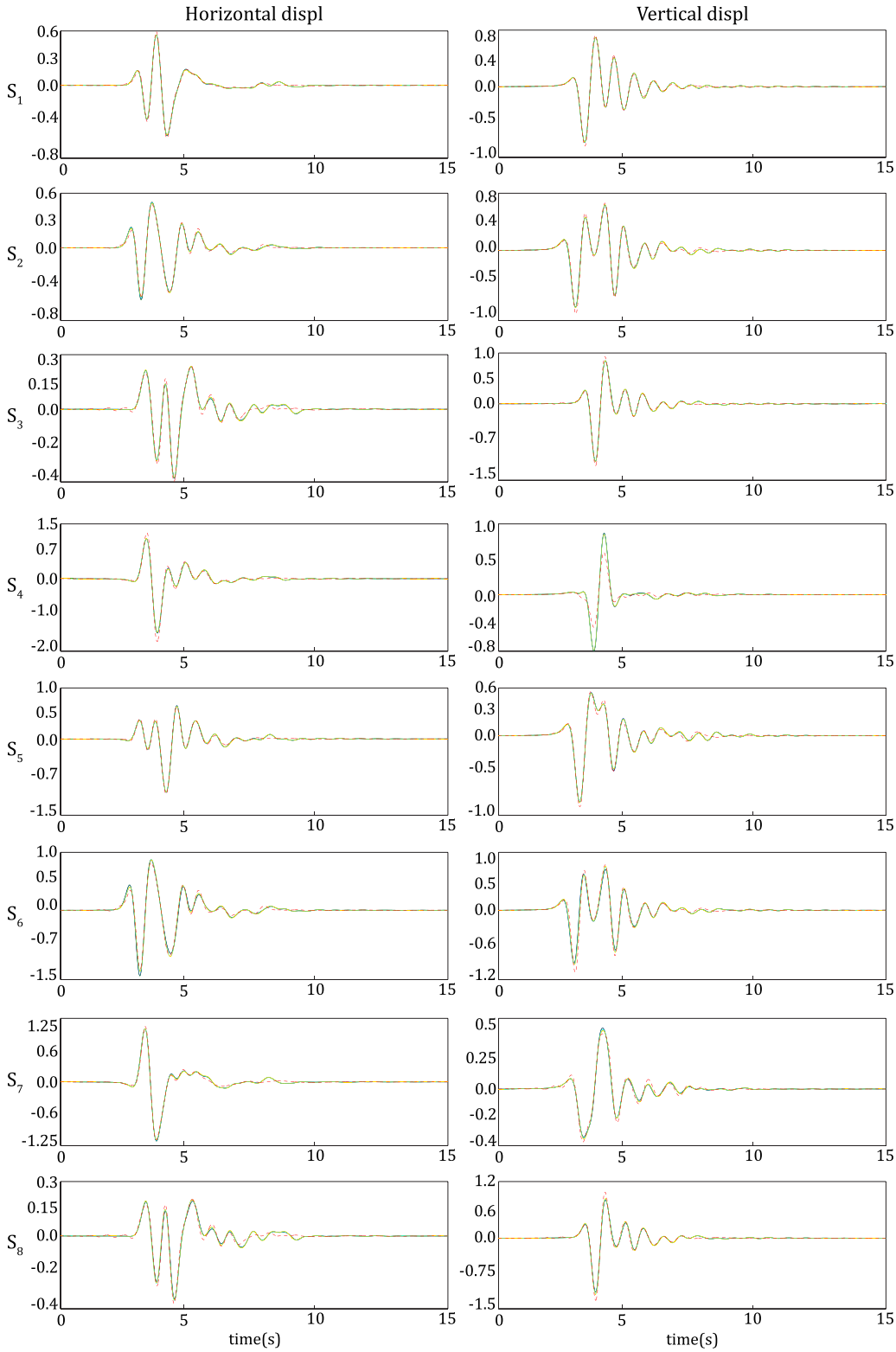

Figure 7. Displacement time histories at stations S1, S2, . . . , S8 throughout the semi-circular homogeneous hill. Blue lines illustrate the results from the 10PPW–4G–25MTR simulation. Similarly, green lines represent results from the 10PPW–8G–12.5MTR analysis, while cyan and yellow lines depict findings from the 20PPW–16G–12.5MTR and the 40PPW–16G–12.5MTR mesh conditions, respectively. Dotted red lines show the results from the BEM numerical scheme.

DOI: 10.1002/nme

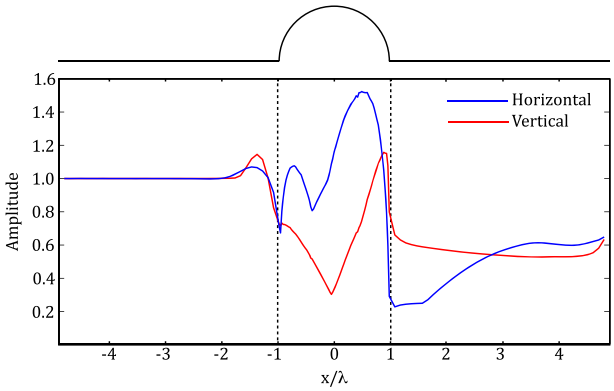

Figure 8. Distribution of peak ground displacement over the free surface of the semi-circular hill over homogeneous half-space. Blue and red lines depict the relative amplification of the horizontal and vertical component of displacement with respect to the components of the incident Rayleigh wave.

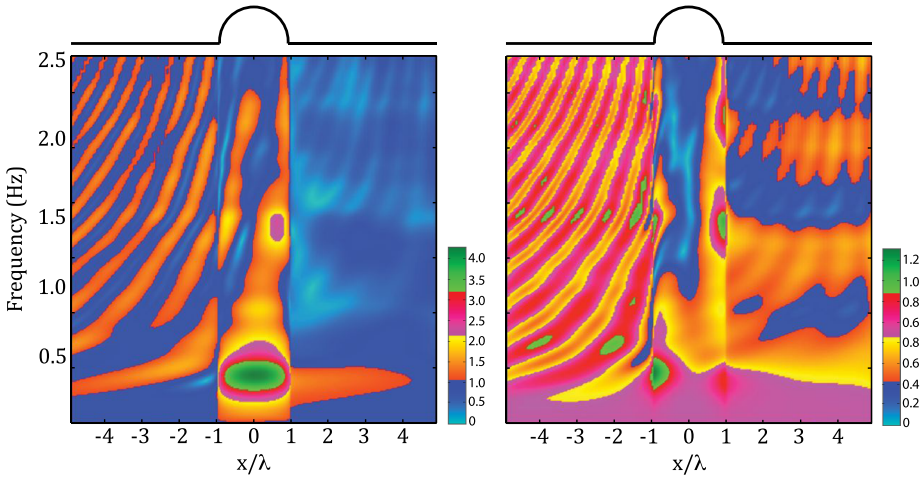

Figure 9. Transfer function amplitudes (TF) as function of position and frequency for both components of displacement. Left figure illustrates the TF amplitudes for the horizontal component of displacement. Right figure represents the TF amplitudes for the vertical component of displacement.

3.2. Semi-circular hill plus parabolic mountain over a homogeneous half-space

The second example consists of an idealized parabolic mountain merged with a semi-circular hill on a homogeneous half-space (Figure 10). An additional source of complexity was introduced in this simulation by including an impedance contrast between the half-space and the surface topography. Figure 11 depicts a magnified view of the 10PPW-4G-25MTR regular FEM mesh for the sub-region of interest. The solid blue line and the red dots represent the targeted surface and the Gauss points used for the numerical integration at the finite elements on the mountain's boundary. Figure 12 shows magnified views near station S8 corresponding to different levels of mesh refinement.

Figures 13 and 14 show a comparison between the synthetics of displacement obtained with the FEM and the BEM schemes for the two components of motion at the selected receivers. Here, all the synthetics exhibit a close agreement. The proposed strategy is capable of reproducing the complex behavior during the entire duration of the ground shaking, including all the main troughs and peaks during the strong phase of the ground shaking and the secondary peaks at the intermediate and final stages of the simulation. Only minor differences arise between FEM results from the different levels of refinement considered. At station S8, for instance, the effects of the sharp geometric variation are reasonably well-captured by the 10PPW-4G-25MTR results in comparison with those from the most refined 40PPW-16G-12.5MTR case.

DOI: 10.1002/nme

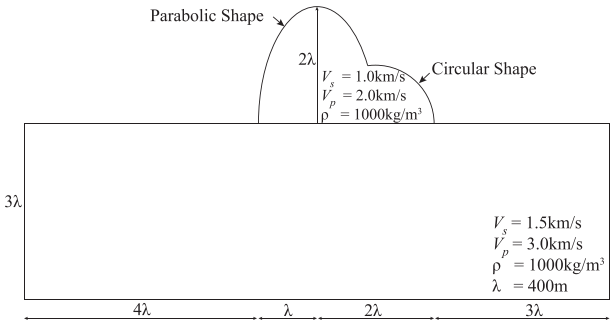

Figure 10. Computational domain for the parabolic ridge and semi-circular hill simulation.

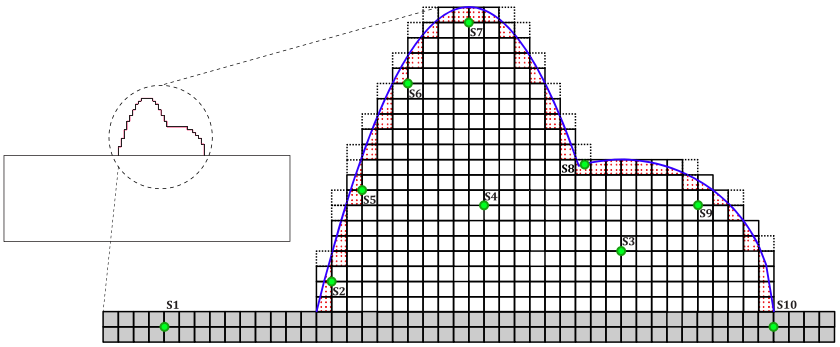

Figure 11. Enlarged view of the 10PPW uniform mesh at the region of interest. Red dots illustrate Gauss points used for the numerical integration at external elements for a 4G Gauss quadrature rule. Dotted black squares represent the disregarded external elements due to the MTR = 25% assumption. Green dots represent the selected internal receivers.

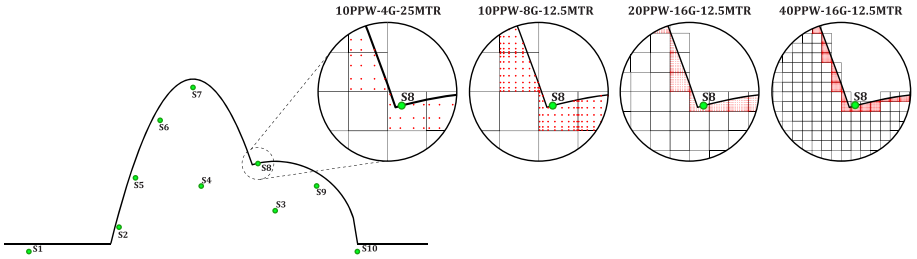

Figure 12. Augmented views of meshes exhibiting different levels of refinement near station S8. The left magnified view depicts a mesh tailor made to accommodate 10 points per wavelength (PPW = 10) in conjunction with a 4 × 4 Gauss quadrature rule (G = 4) and a 25% mass-threshold (MTR = 25%). In the middle-left is the mesh resolution corresponding to PPW = 10, G = 8, and MTR = 12.5%. In the middle-right is the mesh resolution for PPW = 20, G = 16, and MTR = 12.5%. The right view depicts a segment of the PPW = 40, G = 16, MTR = 12.5% mesh in the neighborhood of station S8.

Figures 15 and 16 show the spatial variations of PGD and TF for the two components of motion across the region. In contrast to the previous example, the PGD exhibits a more stable pattern at both sides of the mountain. For $x/\lambda \leqslant -1$, no significant amplifications or reductions take place. For $x/\lambda \geqslant 2$, both components of displacement exhibit reductions with respect to the incident field (vertical = 0.65 and horizontal = 0.40). These reductions are nearly distance independent. The frequency characteristics and spatial PGD changes exhibit a strong variation at the free surface of the mountain. The largest amplification still occurs on the circular ridge, shifted to the right from its top. The values of the amplification, however, differ substantially from the ones in the first example, reaching values as high as 2.2 and 1.6 for the horizontal and vertical components, respec-

DOI: 10.1002/nme

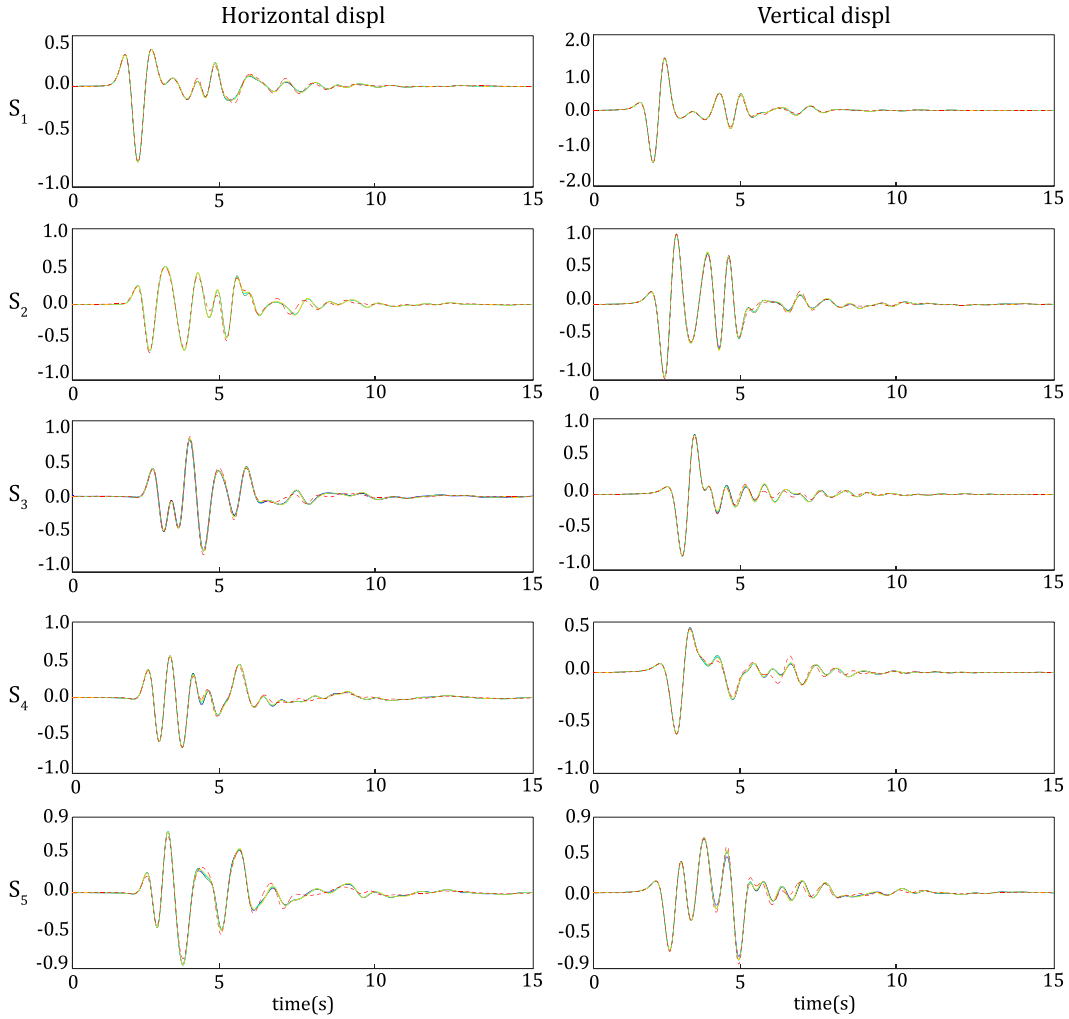

Figure 13. Displacement time histories at the selected stations shown in Figure 11. Blue lines represent results from the 10PPW–4G–25MTR simulation. Green lines represent results from the 10PPW–8G–12.5MTR analysis. Cyan and yellow lines depict findings from the 20PPW–16G–12.5MTR and the 40PPW–16G–12.5MTR mesh conditions, respectively. Red lines show the results from the BEM numerical scheme.

tively. TF results present again a striped pattern across the reflected range, noticeable resonance frequencies at the mountain zone, and a clear shield effect in the transmitted region. In particular, the fundamental frequency for both components of displacement coincide ($f \approx 0.3$ Hz), although with major differences in the amplitude values (Figure 15). Another interesting feature is the broader set of frequencies activated for the vertical motion at the mountain surface where a large cluster of harmonics spans almost the entire parabolic region of the domain.

4. 3D VERIFICATION: VIRTUAL TOPOGRAPHY SCHEME

This section is devoted to analyzing two simple 3D cases in order to illustrate the capabilities of the VT approach. Although we also tried the Gauss integration scheme, the results were significantly less accurate than those obtained using the VT approach. Thus, we present results only from VT, and compare them with solutions previously reported by other authors. Of particular interest will be to examine the performance of the VT compared with topography simulations based upon stair-shaped meshes. Topography modeling based upon staircase meshes is perhaps the simplest strategy

DOI: 10.1002/nme

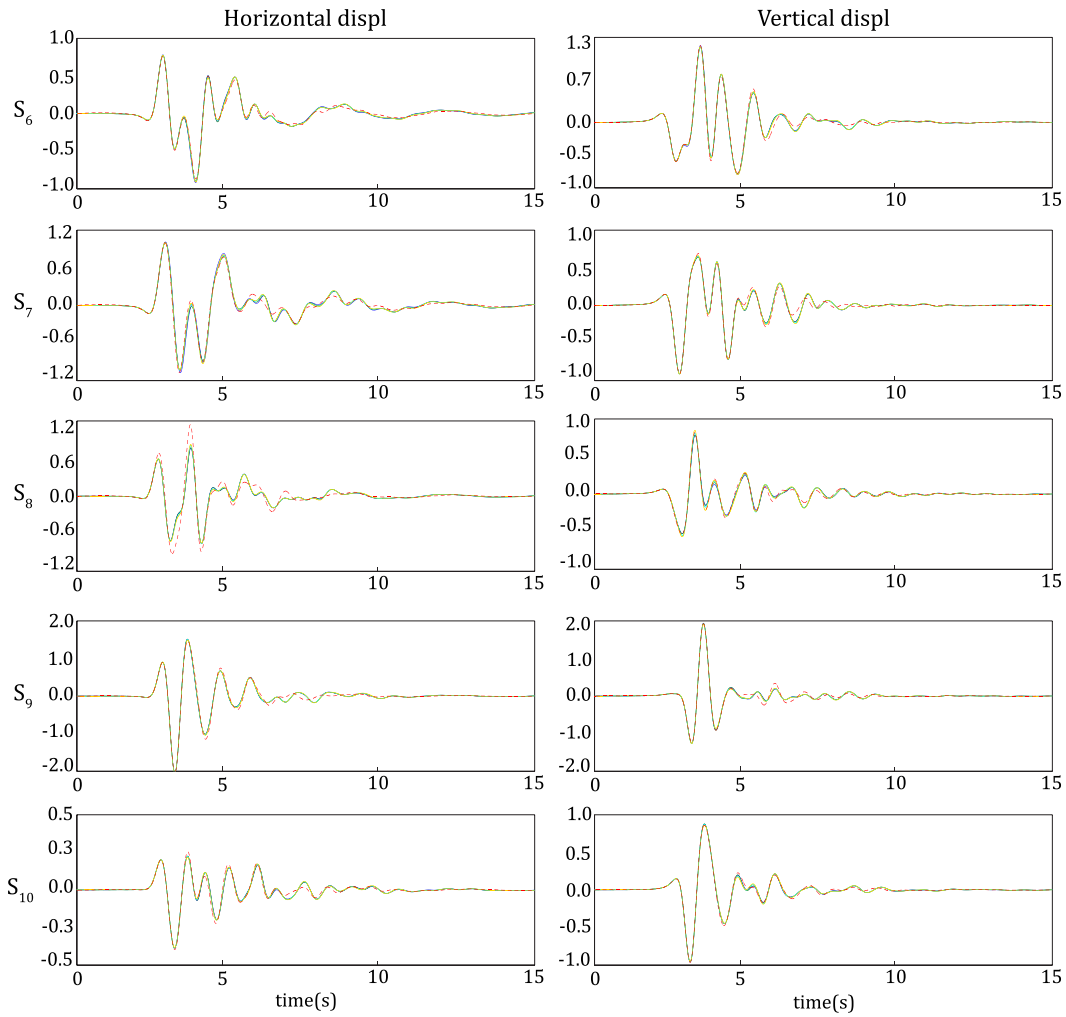

Figure 14. Displacement time histories from station S5 to station S10 of the parabolic mountain plus semi-circular hill example. Blue lines represent results from the 10PPW–4G–25MTR simulation. Green lines illustrate results from the 10PPW–8G–12.5MTR analysis. Cyan and yellow lines depict findings from the 20PPW–16G–12.5MTR and the 40PPW–16G–12.5MTR mesh conditions, respectively. Red doted lines show the results from the BEM numerical scheme.

that one can follow. The inherent idea behind a stair-like approach is that small enough element sizes will automatically lead to accurate results. This idea is by no means wrong, though it might necessitate an excessive mesh refinement. Therefore, quantitative evidence regarding its numerical performance will also be presented, as well as quantitative suggestions of the minimum number of PPW required to assure accurate results.

The performance of the VT approach is examined using two benchmark models; namely, a Gaussian hill subjected to a vertically incident SV-wave, and a Hermitian ridge subjected to a vertically incident P-wave. The material is taken to be homogeneous and without intrinsic damping. Therefore, we use here a single mesh size. In a third example we will consider the effect of near-surface layering to illustrate the application of the more general octree approach with elements of different sizes. In the first two simulations, the effective forces that drive the respective incident wavefields are computed using the Domain Reduction Method (DRM) [46]. In addition to comparing synthetics at different locations, further evidence regarding the numerical performance of the VT approach is presented in terms of convergence tests.

DOI: 10.1002/nme

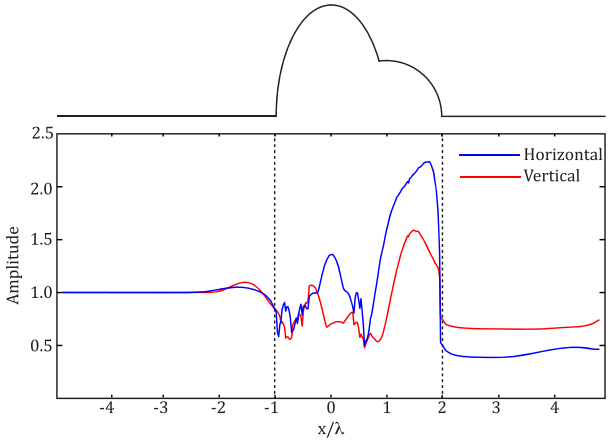

Figure 15. Distribution of peak ground displacement for the parabolic mountain plus semi-circular hill over homogeneous half-space. Blue and red lines depict the relative amplification of the horizontal and vertical component of displacement with respect to the maximum values of the components of the incident Rayleigh wave.

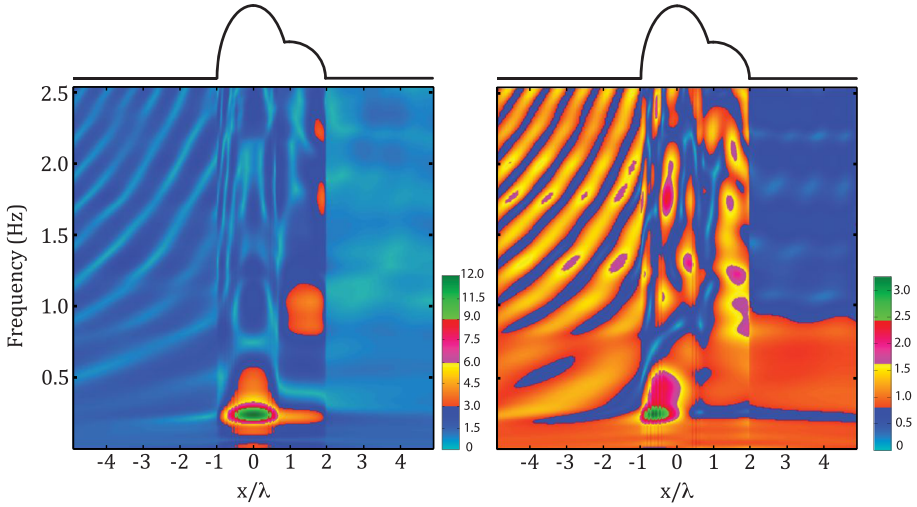

Figure 16. Transfer function amplitudes as function of position and frequency for both components of displacement: horizontal component (left) and vertical component (right).

4.1. Gaussian hill

Figure 17 shows a homogeneous 3D Gaussian hill of elastic material with a P-wave velocity of V_p = 3200 m/s, S-wave V_s = 1847 m/s and density $\rho = 2200\ \text{kg/m}^3$. The seismic source is a vertically incident SV-wave with a Ricker's pulse in time and a central wavelength λ_c = 180 m ($f_c = 10.26Hz$), polarized in the Y direction. The entire computational domain is 2 km × 2 km × 1 km. Results are benchmarked with those reported by [47], which use the spectral element method (SEM).

Synthetics of displacement for receivers placed throughout the minor and major axes of the ridge are presented in Figure 18. The first column corresponds to the results reported by [47]. Results obtained by a traditional staircase mesh for different levels of refinement, that is, 11.52, 23.04, and 46.08PPW are depicted in the second, third, and fourth columns. The last column (fifth column) in Figure 18 presents the synthetics of displacement obtained with the VT approach. A good agreement is exhibited by the VT results when compared with the reference solution. This level of accuracy was obtained with the 11.53PPW mesh resolution as for the flat free-surface simulations.

DOI: 10.1002/nme

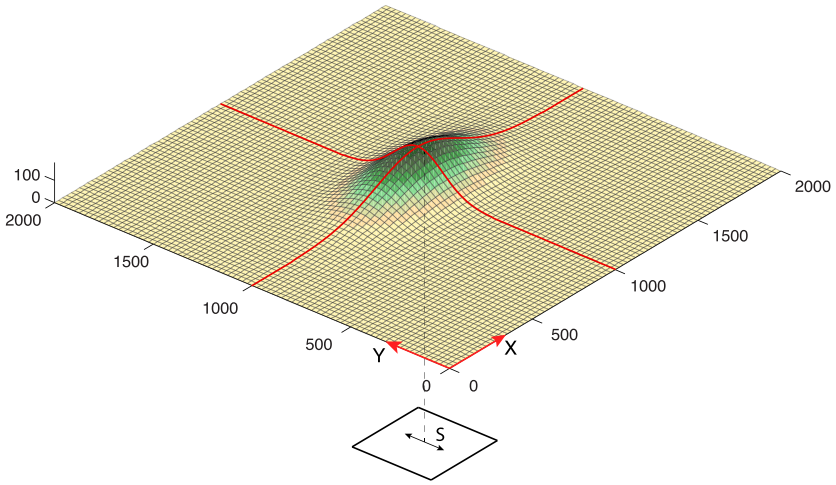

Figure 17. Gaussian mountain subjected to a vertically incident S-wave polarized in the Y direction. The mountain is characterized by $h_o \exp\left(-\frac{(x-x_o)^2}{2\sigma_x^2}\right) \exp\left(-\frac{(y-y_o)^2}{2\sigma_y^2}\right)$, where h_o= 180 m, x_o= 1000 m, y_o= 1000 m, σ_x= 250 m, and σ_y= 125 m.

The two diffracted phases created in the vicinity of the top of the mountain, that is, a P-wave and a Rayleigh-wave, are clearly identified by the VT results (see third row on column 5). In the same vein, the VT results accurately characterize the strong directivity effects exhibited by the 3D geometry of the topography as was pointed out in [47]. On the other hand, results from the staircase approach using the same mesh resolution as in VT, that is, 11.52PPW, exhibit strong artificial phases for every displacement component (see 2nd column of 18). These results are clearly unacceptable. By increasing the refinement of the staircase mesh to 23.04PPW, the amplitude of the artificially diffracted and scattered waves are reduced considerably, although the degradation of the wave fields is still evident. This degradation is more significant in the X and Z components than in the Y component. A further refinement of ∼50PPW finally leads to a satisfactory match between the results of the staircase approach and those from the VT strategy, and from the solution reported in [47].

These results indicate that simulations based upon simple stair-shaped meshes can require up to ∼50PPW in order to obtain an accurate representation of the wavefields. This is in agreement with findings from other studies where exceptionally high refinements are suggested. For instance, [48] reported that in models where the external geometry follows a step-like pattern, the relative error in the Fourier components reaches 35% even for mesh sizes of 1/60th of the minimum wavelength. For simple scenarios, such a level of refinement might not impose a significant constraint, especially with the computational capacity that is currently available. However, because doubling the number of PPW leads to an 8× increment of the topographic elements, while simultaneously reducing by half the required time step of the overall simulation, a staircase mesh tailored to accommodate ∼50PPW would require 64× more external elements than its ∼12PPW counterpart. Additionally, such a mesh would demand a time-step of one-fourth of the original time step. Thus, for end-to-end earthquake simulation, which generally demand vast computational resources, the VT approach becomes greatly advantageous.

4.2. Hermitian ridge

A second example is presented in Figure 19. This problem was previously addressed by [49] using a boundary [49] using a boundary integral equation approach. The topography corresponds to an axisymmetric isolated $h(\xi) = h_o(1 - 3\xi^2 + 2\xi^3)$; $0 < \xi = \frac{r}{r_o} \leqslant 1.$; $h_o = 90$ m; and circular base $r_o = 180$ m. A vertically incident P-wave in the form of a Ricker pulse in time with a central frequency of f_c =10 Hz, is considered as the seismic source. The material properties of both, hill and half-space are: ρ=2200 kg/m^3, $V_p = 3600$ m/s, and Poisson's ratio $\nu = 0.3$. Figure 20 illustrates the VT mesh (∼12PPW) employed in the simulations.

DOI: 10.1002/nme

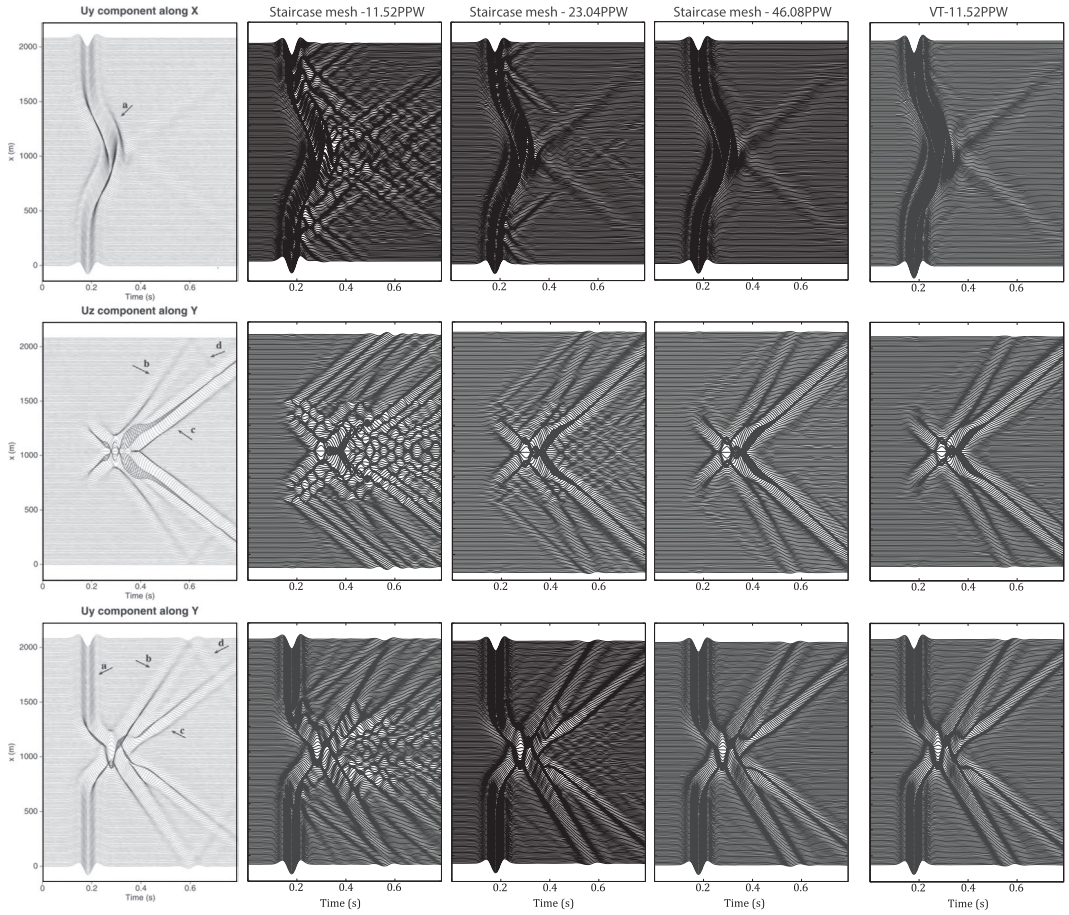

Figure 18. Histories of ground motion displacement from receivers placed at the free-surface of the Gaussian Hill (red lines in Figure 17). First column depicts results reported by [47]. Second, third, and fourth columns represent results from step-like meshes. The last column illustrates the results from the VT non-conforming scheme for a 11.52PPW mesh resolution.

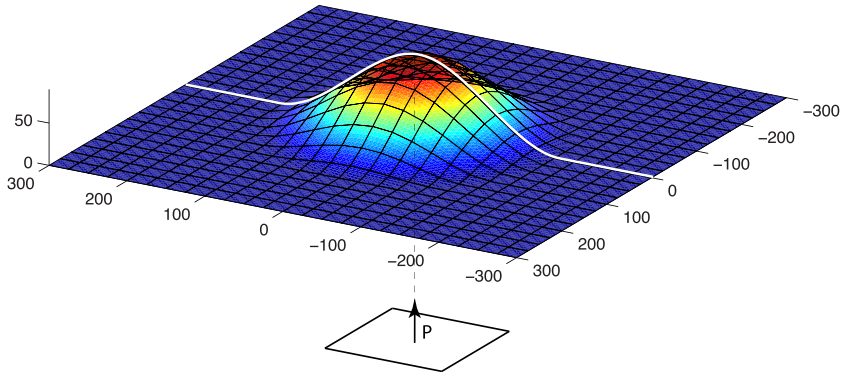

Figure 19. Isolated ridge subjected to a vertically incident P-wave. The ridge is homogeneous with external profile $h_o(1-3\xi^2+2\xi^3)$; $0<\xi=\frac{r}{r_o}\leqslant 1$. $h_o=90$ m; circular base $r_o=180$ m. A vertically incident P-wave as a Ricker pulse in time of $f_c=10$ Hz is considered as the seismic source. The material properties are V_p=3600 m/s and Poisson's ratio $\nu=0.3$.

Reference [49] provided approximate solutions for one specific dimensionless frequency of $\eta_q=r_o/\lambda_p=0.5$, where λ_p represents the wavelength of the incident P-wave. In this verification,

DOI: 10.1002/nme

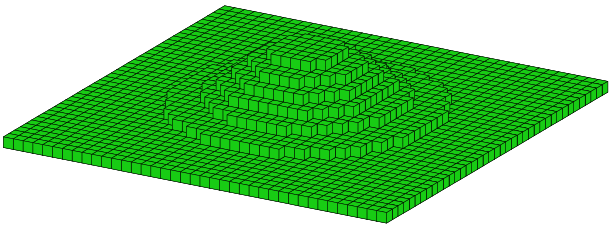

Figure 20. Finite element mesh of ∼12PPW (Δx = 15.625 m) used for the numerical simulation of the isolated Hermitian ridge.

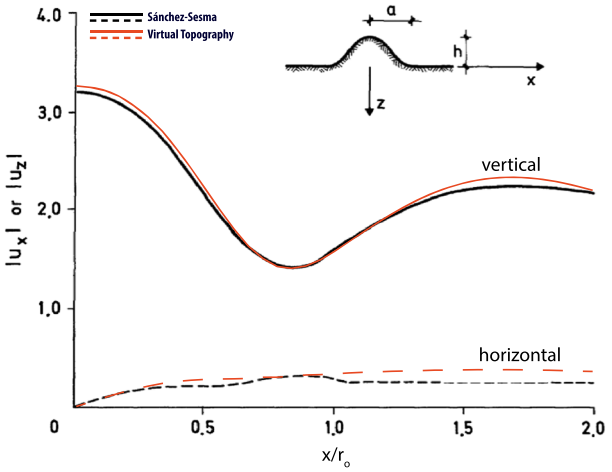

Figure 21. Comparison of the horizontal and vertical Fourier amplitudes at the free-surface of the ridge for a vertically incident P-wave of wavelength $\lambda_p = 720$ m obtained from VT against the approximated results reported by [49]. Results are presented as normalized distances (x/r_o) from the center of the ridge. The Fourier amplitudes come from histories of ground motion recorded at receivers placed along the white line at the free surface of the ridge (Figure 19).

the time histories obtained by the VT scheme were transformed to the frequency domain, and the Fourier amplitudes corresponding to $\lambda_p = 720$m were normalized to compare them with the solutions from [49]. In general, results from both solutions are in good agreement, as shown in Figure 21. Regarding the vertical component, the pattern of amplification is the same for both results, although the VT results are slightly larger than those from the reference solution in the ranges $\approx x/r_o < 0.6$ and $\approx x/r_o > 1.2$. For the horizontal Fourier amplitude, a somewhat larger deviation between the solutions is observed. This might be due to the least-square approximated solution in [49].

A better insight of the characteristics of ground motion is gained by analyzing the VT synthetics of ground motion in Figure 22. In terms of topographic effects, the hill induces modest changes on the free-surface motion. As can be seen, two diffracted phases are created. These are clearly identifiable in the synthetics of the horizontal component. The first phase (arrow a), is a diffracted P-wave. The second diffracted wave is a Rayleigh wave with a $\frac{1}{\sqrt{r}}$ decay. At the top of the hill the Rayleigh wave exhibits the maximum vertical amplitude. This amplitude reaches 1.3× the free-field amplitude. Notice that with the VT approach there is no indication of any artificially generated phases in the displacement waveforms.

4.3. Convergence analysis

The foregoing results have provided evidence that the VT approach properly predicts the most important features of earthquake-induced ground motion. There still remains, however, to corroborate the overall performance of the methodology. We need to answer questions such as how fine must the mesh be in order to provide an acceptable representation of the solution. Unfortunately, there are no analytical solutions available for any 3D elastodynamic problems with surface topography; thus,

DOI: 10.1002/nme

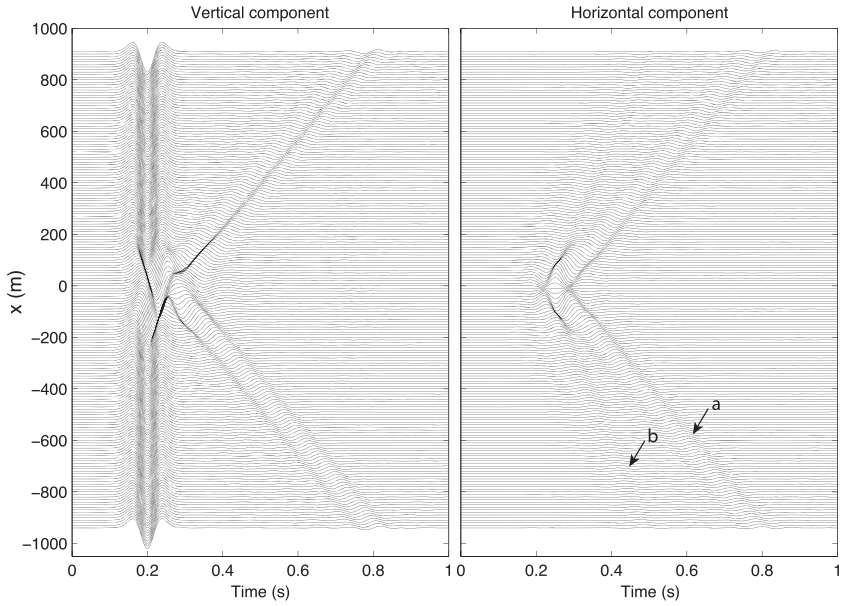

Figure 22. Synthetics of displacement at receivers placed at the surface of the Hermitian ridge along the white line shown in Figure 19. At the top of the ridge, two diffracted phases are created, a Rayleigh-wave (arrow a) and a P-wave (arrow b).

any attempt to compute exactly the error of the VT approach is not possible. Fortunately, the exact quantitative evaluation of the numerical error is not essential for measuring the performance of our numerical approach, as it is possible to estimate numerically the convergence rate of the methodology by considering the numerical solutions for increasingly finer hierarchical meshes. Here we obtain the convergence rates of the VT methodology and compare them with those of the staircase methodology for the two 3D examples considered, following the procedure described by [50]. This technique allows one to compute convergence rates even in the absence of an exact solution. The results shown in Figure 23 were obtained by computing the root-mean-square pairwise difference of the ground motion on the free-surface in the L2-norm, in space and time for two consecutive simulations with decreasing mesh size. To estimate the error we obtained the spatial distribution of the displacement at the free surface, from a hierarchical sequence of five simulations, each one conducted by doubling the number of PPW from the previous one. The starting and final meshes correspond to regular grids with $\sim$5PPW, and $\sim$80PPW respectively.

The convergence rates vary according to a power law of the form $c\,\Delta x^{-\kappa}$, where c is a constant, and κ is the convergence rate. The faster convergence of the VT approach is shown clearly in Figure 23, and Table II.

Table II. Convergence rates for the VT and the Staircase-meshes for the Gaussian hill and the Hermitian ridge, respectively.

	Gaussian mountain		Hermitian ridge	
Method	c	κ	c	κ
VT	6.2×10^{-8}	2.2	5.6×10^{-8}	1.8
Staircase mesh	1.5×10^{-6}	1.3	1.12×10^{-6}	0.88

Contrary to the staircase approach, which exhibits a deterioration of the theoretical convergence rate, the convergence rate of the VT in both simulations remains very close to the theoretical value of 2 expected from the use of trilinear elements in space and second-order central differences in time. By contrast, the staircase approach converges only at a rate of 1.3, and 0.88 for the two geometries

DOI: 10.1002/nme

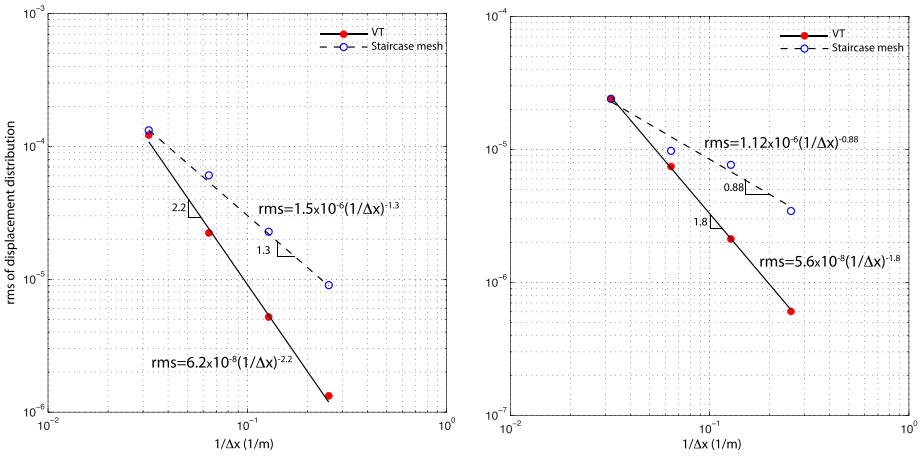

Figure 23. Root-mean-square (rms) error of surface ground motion versus the inverse of the element size Δx for the Gaussian Hill (a), and the Hermitian Ridge simulations (b), respectively. In both figures, dotted regression lines and their associated hollow blue circles are the results obtained under staircase-mesh conditions. Similarly, solid black regression lines and red circles correspond to results obtained by employing the VT scheme.

considered. This occurs most likely because the tetrahedral elements of the VT scheme represent the surficial geometry much more efficiently than the cubic elements of the staircase approximation for an increasing number of PPW.

4.4. Layered hill subjected to an isotropic point-source

To examine the VT approach in more realistic scenarios, which call for variable-size elements, we investigate the earthquake response of an axisymmetric Hermitian hill that includes near-surface layered units. Figure 24(a) and (b) depicts the 3D view and the central section cut of the selected domain. The upper layer is characterized by an S-wave velocity of $V_s = 500$ m/s, while the lower layer and the half-space have S-wave velocities of $V_s = 1000$ m/s and $V_s = 2000$ m/s, respectively. The differences in the material properties arise in practice because of weathering of the crust. All the materials have the same Poisson's ratio $\nu = 0.3$ and mass density $\rho = 2000$ kg/m^3. No material damping was considered. The source is modeled as an isotropic point-source. The slip function varies as a Ricker's pulse with an $f_{\max} = 8$Hz.

We examined the layered system by using three increasingly refined octree meshes corresponding to 4PPW, 8PPW, and 16PPW, respectively (Figure 25(a)). A fourth simulation in which the second layer was refined up to 32PPW was performed as a reference solution for stress analysis (Figure 25(b)). To maintain the continuity of the displacements across elements of different sizes, we constrain the hanging nodes by computing their displacements as appropriate averages of the displacements of its anchored neighbors (e.g., [15]). Near the free-surface, however, where the cubes are divided into tetrahedra, the displacement is continuous only along the edges of the cubes, thus leading to non-conforming elements. Despite the displacement discontinuity at the interfaces, results of our comparisons with the reference solutions in the illustrative examples earlier in this section, and the convergence rates in Figure 23. show that the VT approach provides adequate solutions for the displacements. This most likely is the case because the interfacing cubic-shaped and tetrahedral elements pass the patch test (e.g., [51]).

Figure 26 shows the synthetics of vertical displacement along the free surface. As expected, both low resolution meshes exhibit the poorest results. However, the VT-4PPW results exhibit a much better agreement with the more accurate higher-resolution results than its 4PPW staircase counterpart. Results from the VT-8PPW and the VT-16PPW do not substantially differ from each other. This is an indication that the VT approach provides acceptable results at resolution meshes as low as 8PPW. On the other hand, the 8PPW staircase condition continues to show significant spurious

DOI: 10.1002/nme

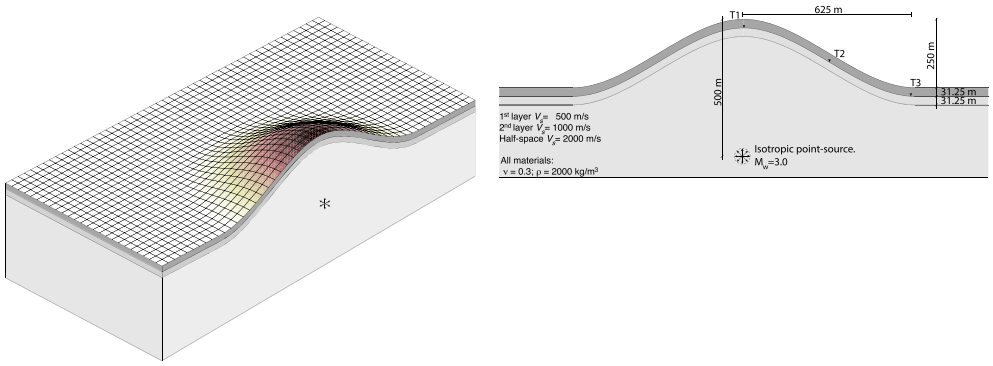

Figure 24. Layered axisymmetric Hermitian hill subjected to an isotropic $M_w = 3.0$ point-source event. (a) 3D view of the targeted domain and location of the isotropic point-source event. The external profile corresponds to $h_o(1 - 3\xi^2 + 2\xi^3)$; $0 < \xi = \frac{r}{r_o} \leqslant 1$. h_o = 250 m; circular base r_o = 625 m. (b) Vertical central section. The hill presents two non-planar lithologic units of shear velocities V_s = 500 m/s, and V_s = 1000 m/s over a homogeneous V_s= 2000 m/s half-space. All the materials share the same density ρ = 2000 kg/m^3, and Poisson's ratio $\nu = 0.3$. T1, T2, and T3 mark the position of material interface stations for stress analysis.

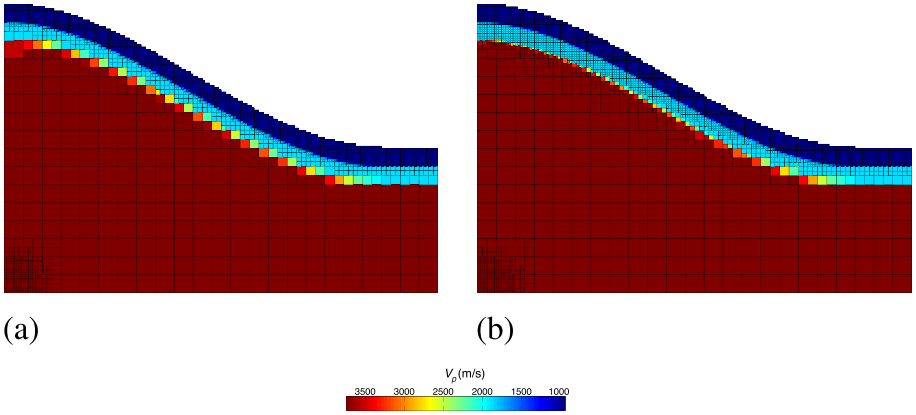

Figure 25. Octree-based meshes. The figures depict right hand side portions of the meshes at the central vertical section down to the hypocenter corresponding to the (a) 16PPW simulation, and the (b) 16/32PPW hybrid simulation, respectively. Colors represent P-wave velocity values.

contributions. Synthetics from the 16PPW staircase simulation reduce considerably artificial contributions, although there are still noticeable diffracted waves originated at the foot of the hill that travel toward the domain's interior.

The main focus of ground motion simulations is on determining the displacements or their time derivatives (velocities, or accelerations) on the free surface. Nonetheless, there are situations in which spatial gradients can be of interest, such as when one is interested in ground motion rotations or nonlinear soil behavior. To examine the VT performance in such situations, we analyze stress time histories at various points of the layered system. Figures 27(a) and (b), and 28 show normal stress synthetics at stations T1, T2, and T3 lying on the first material interface (Figure 24(b)). Blue lines represent results from the staircase condition, red lines those from the VT approach, and dotted black lines depict the reference stress solution obtained using VT with the more refined 16/32PPW mesh shown in Figure 25(b). In general, the VT results are in good agreement with the reference stress solution even at low resolution meshes. As expected, the extent of agreement improves with the mesh resolution. On the other hand, the 4PPW staircase approach significantly deviates from the corresponding benchmark results, though the results improve with mesh refinement. In all cases,

DOI: 10.1002/nme

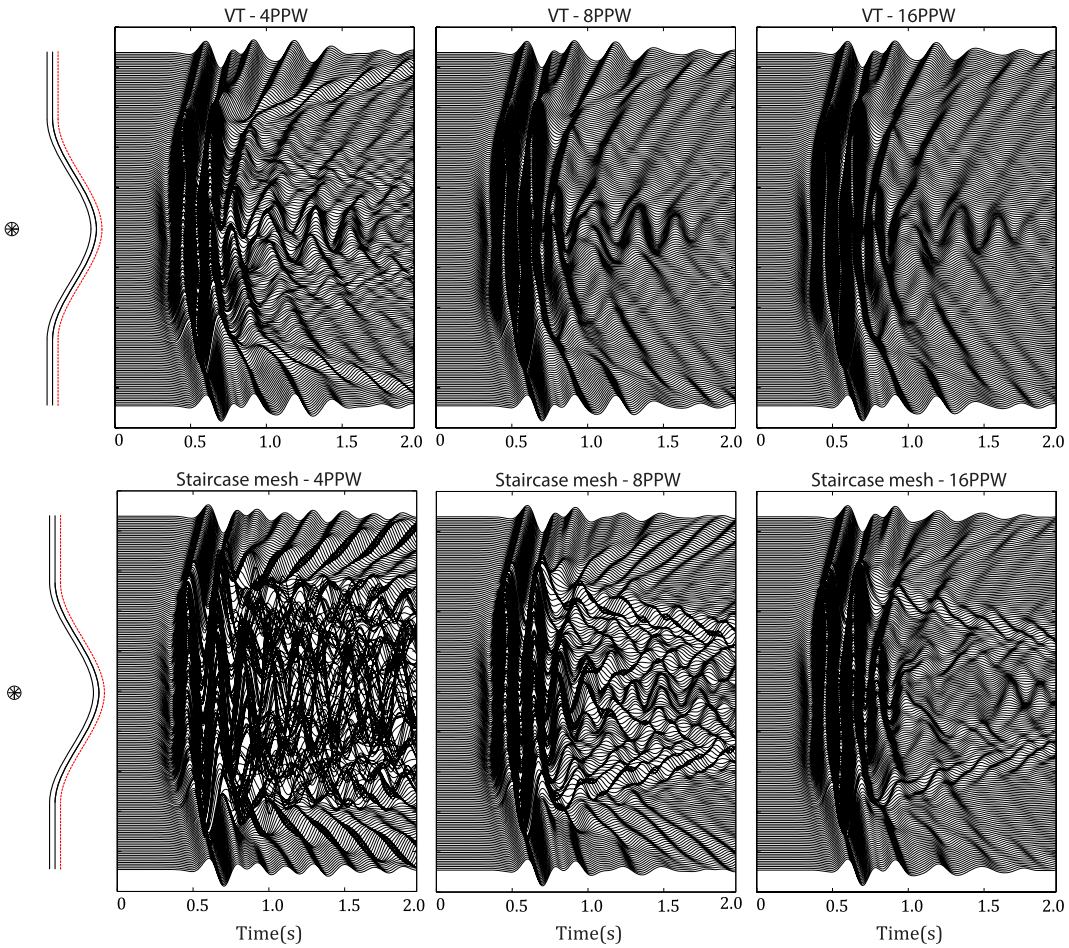

Figure 26. Vertical components of displacement at the free surface (dotted red line) of the layered Hermitian hill.

however, the results of the VT approach are closer to the reference results that those from the staircase approach.

We also calculated the convergence rate for the stresses similarly to what we conducted for the displacements in the earlier examples and found convergence rates as low as 0.4 for the VT methodology for points at the uppermost interface. This degradation of the convergence rate with respect to the theoretical value of unity might be due to the nonconforming nature of the cubic-shaped and the tetrahedra at their interfaces, and to approximating the interior interfaces by a staircase geometry. This aspect of the octree approach is similar to that used in the finite difference method. In fact, a verification [37] of large-scale ground motion simulations in highly heterogeneous media with a flat-free surface, using a fourth-order finite difference method and the present octree finite element approach, shows remarkably similar results for the free surface displacements.

5. CONCLUDING REMARKS

We adopted FD ideas to model realistic topography in end-to-end earthquake ground motion simulations. Specifically, we proposed a modified octree meshing scheme for the numerical representation of the free surface topography. This allowed us to treat localized geometrical variations in free-surface topographic settings. In particular, we proposed a two-step numerical scheme. In the first step, the topography is accommodated by an unstructured octree mesh. This allowed us to use the attractive features of multiresolution cubic-shaped finite elements. In the second step, we subdivide

DOI: 10.1002/nme

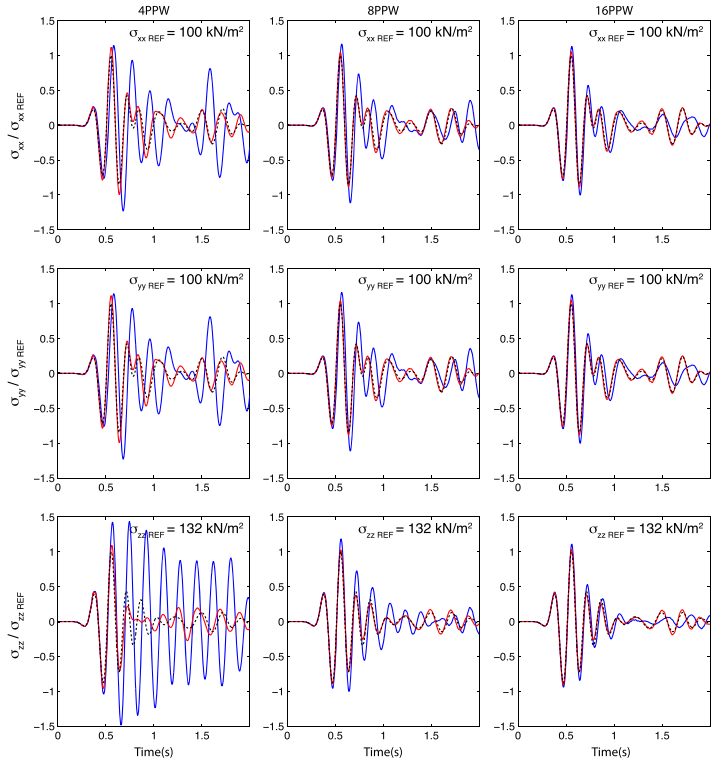

(a)

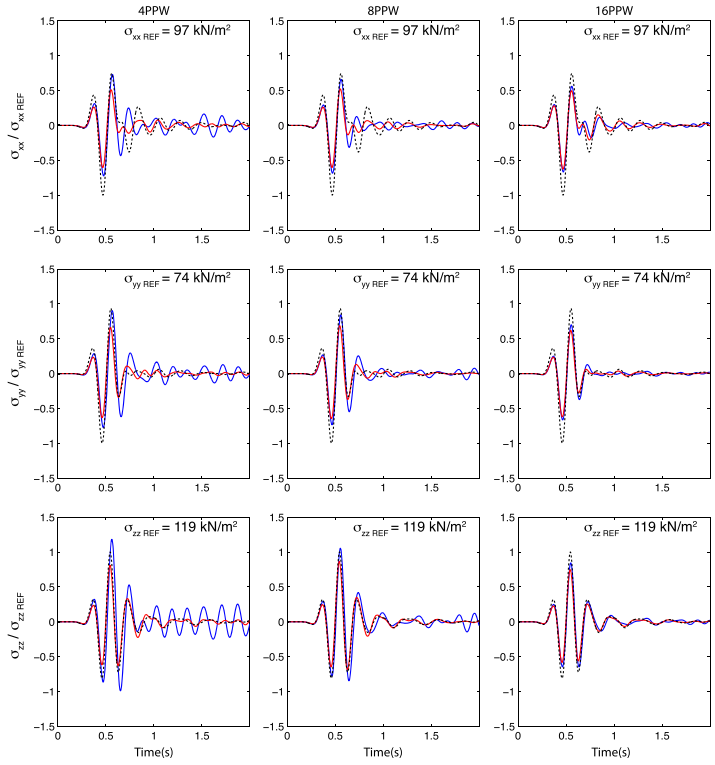

(b)

Figure 27. Normal stress time histories at interface stations T1(a) and T2(b). Blue lines show results from the staircase approximation. Red lines depict VT outcomes. Dotted black lines illustrate results obtained from VT using a 16/32PPW mesh resolution.

DOI: 10.1002/nme

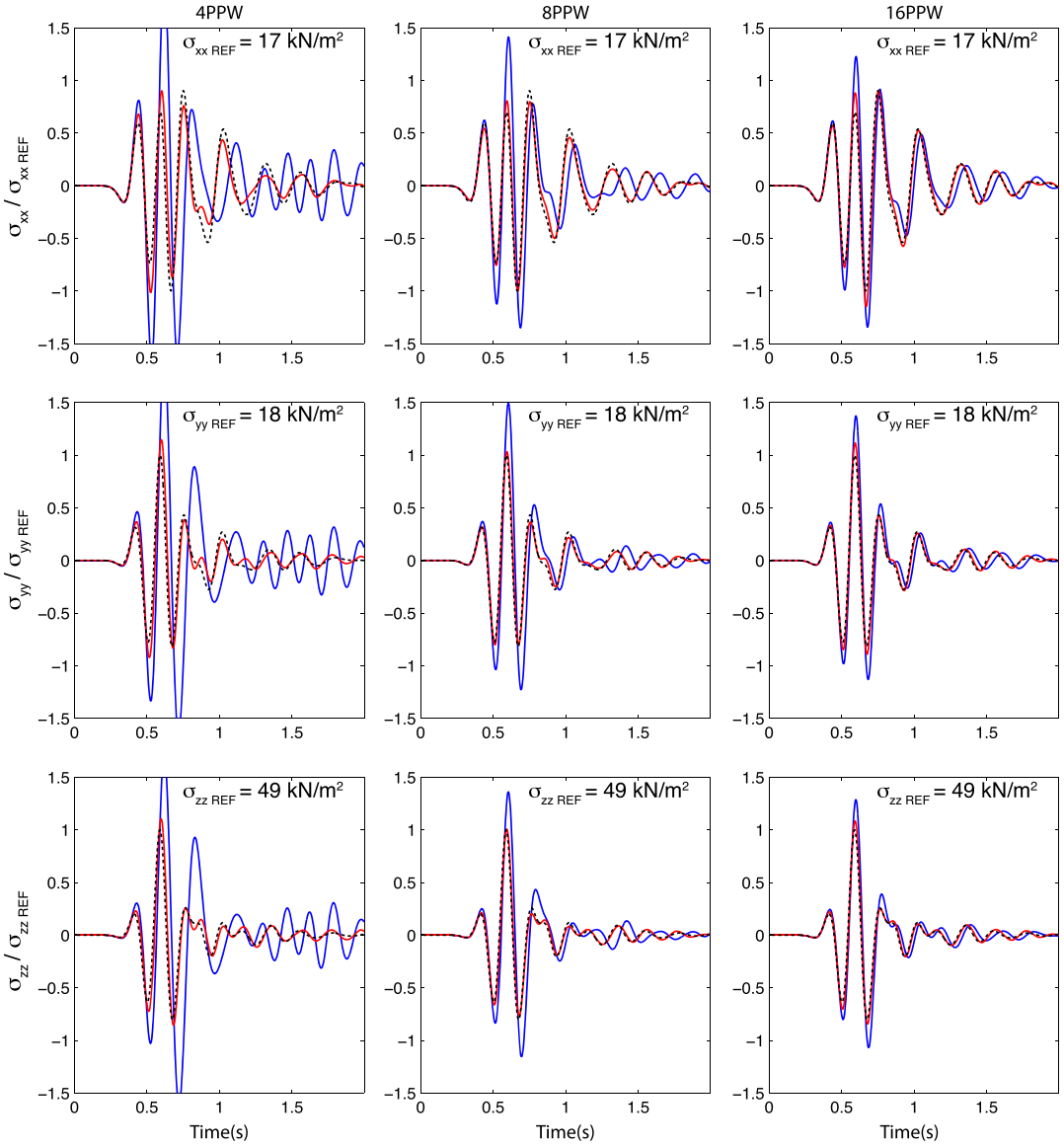

Figure 28. Normal stress time histories at interface station T3 (see Figure 24(b)). Blue lines show results from the staircase approximation. Red lines depict VT outcomes. Dotted black lines illustrate results obtained from VT using a 16/32PPW mesh resolution.

the outer cubic elements into five linear tetrahedral elements. The stiffness matrix of each tetrahedron is scaled according to the topographic volume occupied by the element. The stiffness matrix of the parent cubic finite element is generated by conventional matrix assemblage. Stiffness scalability for the exterior topographic elements is the most prominent feature of the method. Scalability holds, as one needs to compute only five generic stiffness matrices at the beginning of the simulation. Consequently, we showed that the computational advantages of octree-based finite element method are preserved even in the presence of surficial topography, and that the time step required for stability of the problem with surface topography is the same as that for the case of a flat free-surface. We tested the benefits of the VT strategy by benchmarking its results against those from several reference examples including a layered system. Our qualitative comparisons showed a good agreement between the various sets of results. Moreover, the close agreement was obtained using the same mesh refinement as in traditional flat-free surface simulations. In addition, we also verified that staircase meshes can also render acceptable results. However, such meshes require a refinement of up

DOI: 10.1002/nme

50PPW. This is unacceptable for large-scale 3D ground motion simulations. Convergence analysis verified that whereas stairlike meshes lead to significant degradation, the VT approach preserves the convergence rate of the L2-Norm for the displacement field. On the other hand, for the stresses near the free surface, the VT approach converges slower than the theoretical estimates. Thus, for problems for which spatial gradients of the displacements might be of interest, an extension of the VT method to higher-order approximations would be advisable.

ACKNOWLEDGEMENTS

This work was supported by a National Science Foundation (NSF) grant to SCEC:SI2-SSI: A Sustainable Community Software Framework for Petasacale Earthquake Modeling (ACI-1148493), through a Dean's fellowship from the College of Engineering of Carnegie Mellon University (CMU), a Fulbright fellowship from the Colombian Fulbright-Colciencias-DNP program, and additional funding from Universidad EAFIT and the CMU Department of Civil and Environmental Engineering. The SCEC contribution number for this paper is 1934. The computations were performed on Kraken at the U.S. National Institute for Computational Sciences, on Apolo at Universidad EAFIT, and on Blue Waters at NCSA. This research is also part of the Blue Waters Sustained-Petascale Computing project, which is supported by NSF (OCI-0725070) and the state of Illinois. Blue Waters is a joint effort of the University of Illinois at Urbana-Champaign and its National Center for Supercomputing Applications (NCSA). Computational support was possible through a PRAC allocation supported by NSF award: Petascale Research in Earthquake System Science on Blue Waters (PressOnBlueWaters) (NSF ACI-0832698); and the Extreme Science and Engineering Discovery Environment (XSEDE) program supported by NSF (OCI-1053575). We thank Juan Diego Jaramillo of the Universidad EAFIT for providing the boundary element tool used for benchmarking our 2D results. We thank the anonymous reviewers for their helpful comments, suggestions, and careful reading of our work.

REFERENCES

1. Cottrell JA, Hughes TJR, Bazilevs Y. *Isogeometric Analysis: Toward Integration of CAD and FEA*. John Wiley & Sons: Chichester, 2009.
2. Liu GR. *Meshfree Methods: Moving Beyond the Finite Element Method*. CRC press: Boca Raton, 2010.
3. Fernández-Méndez S, Huerta A. Imposing essential boundary conditions in mesh-free methods. *Computer Methods in Applied Mechanics and Engineering* 2004; **193**(12):1257–1275.
4. Bishop J. Rapid stress analysis of geometrically complex domains using implicit meshing. *Computational mechanics* 2003; **30**(5-6):460–478.
5. Belytschko T, Krongauz Y, Fleming M, Organ D, Snm Liu WK. Smoothing and accelerated computations in the element free galerkin method. *Journal of Computational and Applied Mathematics* 1996; **74**(1):111–126.
6. Strouboulis T, Babuška I, Copps K. The design and analysis of the generalized finite element method. *Computer Methods in Applied Mechanics and Engineering* 2000; **181**(1):43–69.
7. Strouboulis T, Copps K, Babuska I. The generalized finite element method: an example of its implementation and illustration of its performance. *International Journal for Numerical Methods in Engineering* 2000; **47**(8):1401–1417.
8. Belytschko T, Black T. Elastic crack growth in finite elements with minimal remeshing. *International Journal for Numerical Methods in Engineering* 1999; **45**(5):601–620.
9. Moës N, Dolbow J, Belytschko T. A finite element method for crack growth without remeshing. *International Journal for Numerical Methods in Engineering* 1999; **46**:131–150.
10. Babuska I, Melenk JM. The partition of unity method. *International Journal for Numerical Methods in Engineering* 1997; **40**(4):727–758.
11. Strouboulis T, Zhang L, Babuška I. Generalized finite element method using mesh-based handbooks: application to problems in domains with many voids. *Computer Methods in Applied Mechanics and Engineering* 2003; **192**(28):3109–3161.
12. Saulev VK. On solution of some boundary value problems on high performance computers by fictitious domain method. *Siberian Mathematical Journal* 1963; **4**(4):912–925 (in Russian).
13. Parvizian J, Düster A, Rank E. Finite cell method. *Computational Mechanics* 2007; **41**(1):121–133.
14. Düster A, Parvizian J, Yang Z, Rank E. The finite cell method for three-dimensional problems of solid mechanics. *Computer Methods in Applied Mechanics and Engineering* 2008; **197**(45):3768–3782.
15. Tu T, Yu H, Ramirez-Guzman L, Bielak J, Ghattas O, Ma KL, O'Hallaron DR. From mesh generation to scientific visualization: An end-to-end approach to parallel supercomputing. *Proceedings of the 2006 ACM/IEEE Conference on Supercomputing,* Tampa, Florida, November 2006; 11–17.

DOI: 10.1002/nme

16. Moës N, Cloirec M, Cartraud P, Remacle JF. A computational approach to handle complex microstructure geometries. *Computer Methods in Applied Mechanics and Engineering* 2003; **192**(28):3163–3177.
17. Toulemonde C, Masson R, El Gharib J. Modeling the effective elastic behavior of composites: a mixed finite element and homogenisation approach. *Comptes Rendus Mécanique* 2008; **336**(3):275–282.
18. Daux C, Moës N, Dolbow J, Sukumar N, Belytschko T. Arbitrary branched and intersecting cracks with the extended finite element method. *International Journal for Numerical Methods in Engineering* 2000; **48**(12):1741–1760.
19. Sukumar N, Chopp DL, Moës N, Belytschko T. Modeling holes and inclusions by level sets in the extended finite-element method. *Computer Methods in Applied Mechanics and Engineering* 2001; **190**(46):6183–6200.
20. Zohdi TI, Wriggers P. Aspects of the computational testing of the mechanical properties of microheterogeneous material samples. *International Journal for Numerical Methods in Engineering* 2001; **50**(11):2573–2599.
21. Zohdi TI, Wriggers P. *An Introduction to Computational Micromechanics. Lecture Notes in Applied and Computational Mechanics*, Vol. 20. Springer: Berlin, 2008.
22. Tran AB, Yvonnet J, He QC, Toulemonde C, Sanahuja J. A multiple level set approach to prevent numerical artefacts in complex microstructures with nearby inclusions within XFEM. *International Journal for Numerical Methods in Engineering* 2011; **85**(11):1436–1459.
23. Fries TP, Belytschko T. The extended/generalized finite element method: An overview of the method and its applications. *International Journal for Numerical Methods in Engineering* 2010; **84**(3):253–304.
24. Bard PY. Diffracted waves and displacement field over two-dimensional elevated topographies. *Geophysical Journal of the Royal Astronomical Society* 1982; **71**(3):731–760.
25. Geli L, Bard PY, Jullien B. The effect of topography on earthquake ground motion: A review and new results. *Bulletin of the Seismological Society of America* 1988; **78**(1):42–63.
26. Sánchez-Sesma FJ, Campillo M. Diffraction of P, SV, and Rayleigh waves by topographic features: A boundary integral formulation. *Bulletin of the Seismological Society of America* 1991; **81**(6):2234–2253.
27. Reinoso E, Wrobel LC, Power H. Three-dimensional scattering of seismic waves from topographical structures. *Soil Dynamics and Earthquake Engineering* 1997; **16**(1):41–61.
28. Allaire G, Jouve F, Toader AM. Structural optimization using sensitivity analysis and a level-set method. *Journal of Computational Physics* 2004; **194**(1):363–393.
29. Bao H, Bielak J, Ghattas O, Kallivokas LF, O'Hallaron DR, Shewchuk JR, Xu J. Large-scale simulation of elastic wave propagation in heterogeneous media on parallel computers. *Computer Methods in Applied Mechanics and Engineering* 1998; **152**:85–102.
30. Moës N, Cloirec M, Cartraud P, Remacle JF. A computational approach to handle complex microstructure geometries. *Computer Methods in Applied Mechanics and Engineering* 2003; **192**(28):3163–3177.
31. Benowitz BA, Waisman H. A spline-based enrichment function for arbitrary inclusions in extended finite element method with applications to finite deformations. *International Journal for Numerical Methods in Engineering* 2013; **95**(5):361–386.
32. Park JH, Choo JF, Cho JR. Dynamic soil-structure interaction analysis for complex soil profiles using unaligned mesh generation and nonlinear modeling approach. *KSCE Journal of Civil Engineering* 2013; **17**(4):753–762.
33. Kim HJ, Swan CC. Algorithms for automated meshing and unit cell analysis of periodic composites with hierarchical tri-quadratic tetrahedral elements. *International Journal for Numerical Methods in Engineering* 2003; **58**(11): 1683–1711.
34. Ichimura T, Hori M, Bielak J. A hybrid multiresolution meshing technique for finite element three-dimensional earthquake ground motion modelling in basins including topography. *Geophysical Journal International* 2009; **177**(3):1221–1232.
35. Graves RW. Simulating seismic wave propagation in 3D elastic media using staggered-grid finite differences. *Bulletin of the Seismological Society of America* 1996; **86**(4):1091–1106.
36. Moczo P, Kristek J, Vavryčuk V, Archuleta RJ, Halada L. 3D heterogeneous staggered-grid finite-difference modeling of seismic motion with volume harmonic and arithmetic averaging of elastic moduli and densities. *Bulletin of the Seismological Society of America* 2002; **92**(8):3042–3066.
37. Bielak J, Graves RW, Olsen KB, Taborda R, Ramírez-Guzmán L, Day SM, Ely GP, Roten D, Jordan TH, Maechling PJ, Urbanic J, Cui Y, Juve G. The ShakeOut earthquake scenario: Verification of three simulation sets. *Geophysical Journal International* 2010; **180**(1):375–404.
38. Menouillard T, Réthoré J, Combescure A, Bung H. Efficient explicit time stepping for the eXtended Finite Element Method (X-FEM). *International Journal for Numerical Methods in Engineering* 2006; **68**(9):911–939.
39. Elguedj T, Gravouil A, Maigre H. An explicit dynamics extended finite element method. Part 1: Mass lumping for arbitrary enrichment functions. *Computer Methods in Applied Mechanics and Engineering* 2009; **198**:2297–2317.
40. Rozycki P, Moës N, Bechet E, Dubois C. X-FEM explicit dynamics for constant strain elements to alleviate mesh constraints on internal or external boundaries. *Computer Methods in Applied Mechanics and Engineering* 2008; **197**(5):349–363.
41. Cupillard P, Delavaud E, Burgos G, Festa G, Vilotte JP, Capdeville Y, Montagner JP. Regsem: a versatile code based on the spectral element method to compute seismic wave propagation at the regional scale. *Geophysical Journal International* 2012; **188**(3):1203–1220.
42. Ma S, Archuleta RJ, Page MT. Effects of large-scale surface topography on ground motions, as demonstrated by a study of the San Gabriel mountains, Los Angeles, California. *Bulletin of the Seismological Society of America* 2007; **97**(6):2066–2079.

DOI: 10.1002/nme

43. Lysmer J, Kuhlemeyer RL. Finite dynamic model for infinite media. *Journal of Engineering Mechanics, ASCE* 1969; **95(EM4)**:859–877.
44. DAMIAN. *A set of computational tools for the simulation of wave propagation problems inelastic solids.* Grupo de Maecánica Aplicada. Research report #002-2013. Universidad EAFIT: Medellin, Colombia, 2013.
45. Bouchon M. Effect of topography on surface motion. *Bulletin of the Seismological Society of America* 1973; **63**(2):615–632.
46. Bielak J, Loukakis K, Hisada Y, Yoshimura C. Domain reduction method for three-dimensional earthquake modeling in localized regions, Part I: Theory. *Bulletin of the Seismological Society of America* 2003; **93**(2):817–824.
47. Komatitsch D, Vilotte JP. The spectral element method: An efficient tool to simulate the seismic response of 2D and 3D geological structures. *Bulletin of the Seismological Society of America* 1998; **88**(2):368–392.
48. Ichimura T, Hori M, Kuwamoto H. Earthquake motion simulation with multiscale finite-element analysis on hybrid grid. *Bulletin of the Seismological Society of America* 2007; **97**(4):1133–1143.
49. Sánchez-Sesma FJ. Diffraction of elastic waves by three-dimensional surface irregularities. *Bulletin of the Seismological Society of America* 1983; **73**(6A):1621–1636.
50. Goto H, Bielak J. Galerkin boundary integral equation method for spontaneous rupture propagation problems: SH-case. *Geophysical Journal International* 2008; **172**(3):1083–1103.
51. Hughes TJR. *The Finite Element Method: Linear Static and Dynamic Finite Element Analysis*. Dover Publications: Mineola, NY, 2000.

DOI: 10.1002/nme